

A quantum information processor with trapped ions

**Philipp Schindler¹, Daniel Nigg¹, Thomas Monz¹, Julio T. Barreiro¹,
Esteban Martinez¹, Shannon X. Wang², Stephan Quint¹, Matthias F. Brandl¹
Volckmar Nebendahl³, Christian F. Roos⁴, Michael Chwalla^{1,4}, Markus Hennrich¹
and Rainer Blatt^{1,4}**

¹Institut für Experimentalphysik, Universität Innsbruck, Technikerstrasse 25, A-6020 Innsbruck, Austria

²Massachusetts Institute of Technology, Center for Ultracold Atoms, Department of Physics, 77
Massachusetts Avenue, Cambridge, MA, 02139, USA

³Institut für Theoretische Physik, Universität Innsbruck, Technikerstrasse 25, A-6020 Innsbruck, Austria

⁴Institut für Quantenoptik und Quanteninformation der Österreichischen Akademie der Wissenschaften,
Technikerstrasse 21a, A-6020 Innsbruck, Austria

Abstract. Quantum computers hold the promise to solve certain problems exponentially faster than their classical counterparts. Trapped atomic ions are among the physical systems in which building such a computing device seems viable. In this work we present a small-scale quantum information processor based on a string of $^{40}\text{Ca}^+$ ions confined in a macroscopic linear Paul trap. We review our set of operations which includes non-coherent operations allowing us to realize arbitrary Markovian processes. In order to build a larger quantum information processor it is mandatory to reduce the error rate of the available operations which is only possible if the physics of the noise processes is well understood. We identify the dominant noise sources in our system and discuss their effects on different algorithms. Finally we demonstrate how our entire set of operations can be used to facilitate the implementation of algorithms by examples of the quantum Fourier transform and the quantum order finding algorithm.

Contents

1	Tools for quantum information processing in ion traps	3
1.1	Quantum information processing in ion traps	3
1.2	The qubit - $^{40}\text{Ca}^+$	3
1.3	The universal set of gates	6
1.4	Optimized sequences of operations	8
1.5	Tools beyond coherent operations	9
2	Experimental setup	11
2.1	The linear Paul trap	11

<i>CONTENTS</i>	2
2.2 Optical setup	12
2.3 Experiment control	14
2.4 Measuring individual ions within a quantum register	15
3 Error sources	18
3.1 Errors in the qubit memory	19
3.2 Errors in quantum operations	22
3.2.1 Initialization	22
3.2.2 Coherent manipulation	24
3.2.3 Measurement	26
3.3 Estimating the effect of noise on an algorithm	26
4 Example algorithms	28
5 Conclusion and Outlook	32
6 Appendix	36

1. Tools for quantum information processing in ion traps

1.1. Quantum information processing in ion traps

A quantum computer (QC) hold the promise to solve certain problems exponentially faster than any classical computer. Its development was boosted by the discovery of Shor's algorithm to factorize large numbers and the insight that quantum error correction allows arbitrary long algorithms even in a noisy environment [1–4]. These findings initiated major experimental efforts to realize such a quantum computer in different physical systems [5–7]. One of the most promising approaches utilizes single ionized atoms confined in Paul traps. Here, the internal state of each ion represents the smallest unit of quantum information (a qubit). Multiple qubit registers are realized by a linear ion string and the interaction between different ions along the string is mediated by the Coulomb interaction [8–10]. In this work we present a review of a small scale quantum information processor based on a macroscopic linear Paul trap [11]. The work is structured as follows: The first section summarizes the available coherent and non-coherent operations and in section 2 the experimental setup is reviewed. In section 3 the noise sources are characterized, and finally, in section 4 we discuss examples of implemented algorithms that use the full set of operations.

1.2. The qubit - $^{40}\text{Ca}^+$

A crucial choice for any QC implementation is the encoding of a qubit in a physical system. In ion trap based QCs, two distinct types of qubit implementations have been explored: (i) ground-state qubits where the information is encoded in two hyperfine or Zeeman sublevels of the ground state [9], and (ii) optical qubits where the information is encoded in the ground state and an optically accessible metastable excited state [11]. The two types of qubits require distinct experimental techniques where, in particular, ground-state qubits are manipulated with either two-photon Raman transitions or by direct microwave excitation [9]. In contrast, operations on optical qubits are performed via a resonant light field provided by a laser [11, 12]. Measuring the state of the qubits in a register is usually performed by the electron shelving method using an auxiliary short-lived state for both qubit types [9]. In the presented setup we use $^{40}\text{Ca}^+$ ions, which contain both, an optical qubit for state manipulation and a ground-state qubit for a quantum memory. Figure 1a) shows a reduced level scheme of $^{40}\text{Ca}^+$ including all relevant energy levels.

Our standard qubit is encoded in the $4S_{1/2}$ ground state and the $3D_{5/2}$ metastable state, where the natural lifetime of the $3D_{5/2}$ state ($\tau_1 = 1.1\text{s}$) provides an upper limit to the storage time of the quantum information. The $4S_{1/2}$ state consists of two Zeeman sublevels ($m = \pm 1/2$) whereas the $3D_{5/2}$ state has six sublevels ($m = \pm 1/2, \pm 3/2, \pm 5/2$). This leads to ten allowed optical transitions given the constraint that only $\Delta m = 0, 1, 2$ are possible on a quadrupole transition. The coupling strength on the different transitions can be adjusted by varying the polarization of the light beam and its angle of incidence with respect to the quantization axis set by the direction of the applied magnetic field. Usually we choose the $4S_{1/2}(m_j = -1/2) = |S\rangle = |1\rangle$ and the $3D_{5/2}(m_j = -1/2) = |D\rangle = |0\rangle$ as the computational basis states because the transition connecting them is the least sensitive to fluctuations in

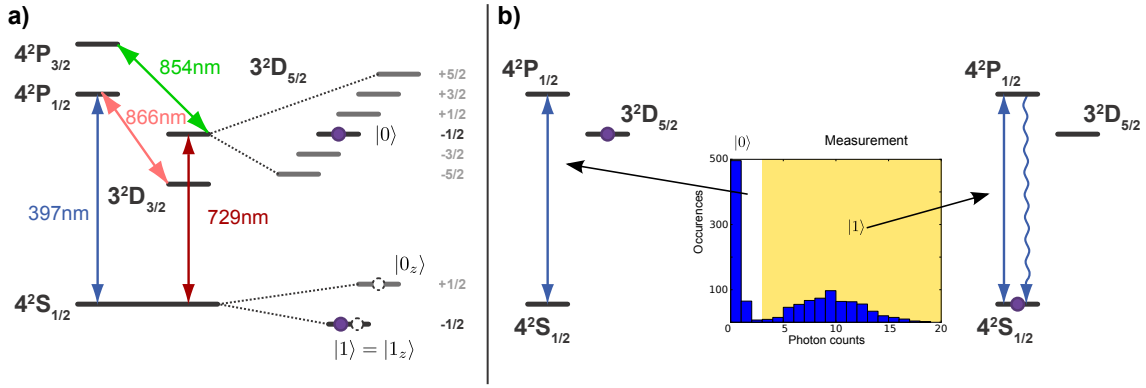


Figure 1. (a) Level scheme of $^{40}\text{Ca}^+$. Solid circles indicate the usual optical qubit ($4S_{1/2}(m_j = -1/2) = |1\rangle$ and $3D_{5/2}(m_j = -1/2) = |0\rangle$). Open circles indicate the ground state qubit which is not subject to spontaneous decay ($4S_{1/2}(m_j = -1/2) = |1\rangle_Z$ and $4S_{1/2}(m_j = +1/2) = |0\rangle_Z$). (b) Schematic representation of electron shelving detection. The histogram shows the detected photon counts from projections onto both states during the detection interval. It can be seen that it is possible to distinguish the two different outcomes. The highlighted area illustrates the threshold whether the state is detected as $|0\rangle$ or $|1\rangle$.

the magnetic field. Furthermore it is possible to store quantum information in the two Zeeman substates of the $4S_{1/2}$ ground-state which are not subject to spontaneous decay: $4S_{1/2}(m_j = -1/2) = |1\rangle_Z$ and $4S_{1/2}(m_j = +1/2) = |0\rangle_Z$.

The projective measurement of the qubit in the computational basis is performed via excitation of the $4S_{1/2} \leftrightarrow 4P_{1/2}$ transition at a wavelength of 397nm. If the qubit is in a superposition of the qubit states, shining in a near resonant laser at the detection transition projects the ion's state either in the $4S_{1/2}$ or the $3D_{5/2}$ state. If the ion is projected into the $4S_{1/2}$ state, a closed cycle transition is possible and the ion will fluoresce as sketched in figure 1(b). It is however still possible that the decay from $4P_{1/2}$ leads to population being trapped in the $3D_{3/2}$ state that needs to be pumped back to the $4P_{1/2}$ with light at 866nm (b). Fluorescence is then collected with high numerical aperture optics and single-photon counting devices as described in section 2. If the ion is projected into the $3D_{5/2}$ state though, it does not interact with the light field and no photons are scattered. Thus the absence or presence of scattered photons can be interpreted as the two possible measurement outcomes which can be clearly distinguished as shown in the histogram in figure 1(b). In order to measure the probability $p_{|1\rangle}$ to find the qubit in $4S_{1/2}$, this measurement needs to be performed on multiple copies of the same state. In ion-trap QCs these multiple copies are produced by repeating the experimental procedure N times yielding the probability $p_{|1\rangle} = n(|1\rangle)/N$ where $n(|1\rangle)$ is the number of bright outcomes. This procedure has a statistical uncertainty given by the projection noise $\Delta p_{|1\rangle} = \sqrt{p_{|1\rangle}(1-p_{|1\rangle})/N}$ [13]. Depending on the required precision, the sequence is therefore executed between 50 and 5000 times.

Preparing the qubit register in a well defined state is a crucial prerequisite of any quantum computer. In our system this means (i) preparing the qubit in one of the two Zeeman levels of the ground state and (ii) cooling the motional state of the ion string in the trap to the ground state. The well established technique of optical pumping is used to prepare each ion in the $m_j = -1/2$ state of the $4S_{1/2}$ state [11]. In our setup two distinct methods for optical pumping are available: (i) Polarization dependent optical pumping by a circularly polarized laser beam resonant on the $4S_{1/2} \leftrightarrow 4P_{1/2}$ transition as shown in figure 2(a) and

(ii) frequency selective optical pumping via the Zeeman substructure of the $3D_{5/2}$ state as depicted in figure 2b). Here, the transfer on the qubit transition at 729 nm is frequency selective. Selection rules ensure that depletion of the $3D_{5/2}(m_j = -3/2)$ level via the $4P_{3/2}$ effectively pumps the population into the $4S_{1/2}(m_j = -1/2)$ state. The second part of the initialization procedure prepares the ion string in

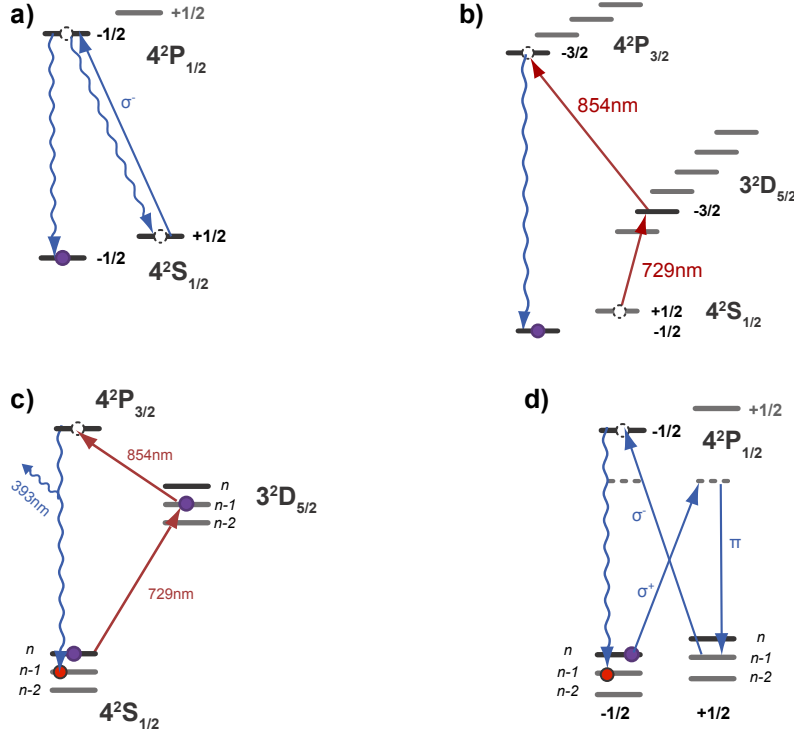


Figure 2. Schematic view of optical pumping which is (a) polarization selective and (b) frequency selective (c) Sideband cooling on the qubit transition. The light resonant with the $3D_{5/2} \rightarrow 4P_{3/2}$ transition is used to tune the effective linewidth of the excited state leading to an adiabatic elimination of the $3D_{5/2}$ state. (d) Scheme for sideband cooling utilizing a Raman transition. Here, the σ^- light performs optical pumping which corresponds to the spontaneous decay on the optical transition.

the motional ground state which requires multiple laser-cooling techniques. We use a two-step process where the first step consists of Doppler cooling on the $4S_{1/2} \leftrightarrow 4P_{1/2}$ transition leading to a mean phonon number of $\langle n \rangle \approx 10$. The motional ground state is subsequently reached with sideband cooling techniques [14]. In our system, the necessary two-level system can be either realized on the narrow qubit transition [15] or as a Raman process between the two ground states via the $4P_{1/2}$ level [9, 11]. A crucial parameter, determining the cooling rate, is the linewidth of the actual cooling transition [14]. When cooling on the long-lived optical transition, the excited state lifetime needs to be artificially shortened in order to adjust the effective linewidth of the transition. This is realized by repumping population from the $3D_{5/2}$ state to the $4S_{1/2}$ state via the $4P_{3/2}$ level with light at 854nm, as outlined in figure 2c) [14]. The procedure using the Raman transition is outlined in figure 2d). Here, the spontaneous decay is replaced by optical pumping as used for state preparation [9, 16]. In principle, this cooling technique allows for faster cooling rates as the coupling strength to the motional mode, described by the Lamb-Dicke parameter, increases for smaller wavelengths. More importantly, it has the advantage of being applicable within a quantum algorithm without disturbing the quantum state of idling qubits when the population of the $4S_{1/2}(m_j = -1/2) = |0\rangle$ state is transferred to a Zeeman substate of the excited state that is outside the

computational basis, for example $3D_{5/2}(m_j = -5/2) = |D'\rangle$ [17].

1.3. The universal set of gates

With a universal set of gates at hand, every unitary operation acting on a quantum register can be implemented [18]. The most prominent example for such a set consists of arbitrary single-qubit operations and the controlled NOT (CNOT) operation. However, depending on the actual physical system, the CNOT operation may be unfavorable to implement and thus it may be preferable to choose a different set of gates. In current ion trap systems, entangling operations based on the ideas of Mølmer and Sørensen have achieved the highest fidelities [19–21]. These gates, in conjunction with single-qubit operations, form a universal set of gates. In order to implement all necessary operations, we use a wide laser beam to illuminate globally the entire register uniformly and a second, tightly focused, steerable laser beam to address each ion. Interferometric stability between the two beams would be required, if arbitrary single-qubit operations were performed with this addressed beam in addition to the global operations. To circumvent this demanding requirement, the addressed beam is only used for inducing phase shifts caused by the AC-Stark effect. Using such an off-resonant light has the advantage that the phase of the light field does not affect the operations and thus no interferometric stability is needed. The orientation of the two required laser beams is shown in figure 3a).

Applying an off-resonant laser light with Rabi frequency Ω and detuning δ onto a the j -th ion modifies its qubit transition frequency by an AC-Stark shift of $\delta_{AC} = -\frac{\Omega^2}{2\Delta}$. This energy shift causes rotations around the Z axis of the Bloch sphere and the corresponding operations on ion j can be expressed as

$$S_z^{(j)}(\theta) = e^{-i\theta\sigma_z^{(j)}/2}$$

where the rotation angle $\theta = \delta_{AC}t$ is determined by the AC-Stark shift and the pulse duration. As the $^{40}\text{Ca}^+$ ion is not a two-level system, the effective frequency shift originates from AC-Stark shifts on multiple transitions. We choose the laser frequency detuning from any $4S_{1/2} \leftrightarrow 3D_{5/2}$ transition to be 20MHz. There, the dominating part of the AC-Stark shift originates from coupling the far off-resonant transitions from $4S_{1/2}$ to $4P_{1/2}$ and $4P_{3/2}$ as well as from $3D_{5/2}$ to $4P_{3/2}$ [22].

The second type of non-entangling operations are collective resonant operations using the global beam. They are described by

$$R_\phi(\theta) = e^{-i\theta S_\phi/2}$$

where $S_\phi = \sum_{i=0}^N (\sigma_x^{(i)} \cos \phi + \sigma_y^{(i)} \sin \phi)$ is the sum over all single-qubit Pauli matrices $\sigma_{x,y}^{(i)}$ acting on qubit i . The rotation axis on the Bloch sphere ϕ is determined by the phase of the light field and the rotation angle $\theta = t\Omega$ is fixed by the pulse duration t and the Rabi frequency Ω . Together with the single-qubit operations described above this set allows us to implement arbitrary non-entangling operations on the entire register.

The entangling MS gate operation completes the universal set of operations. The ideal action of the gate on an N-qubit register is described by

$$MS_\phi(\theta) = e^{-i\theta S_\phi^2/4} .$$

For any even number of qubits the operation $MS_\phi(\pi/2)$ maps the ground state $|00\dots 0\rangle$ directly onto the maximally entangled GHZ state $1/\sqrt{2}(|00\dots 0\rangle - i e^{iN\phi}|11\dots 1\rangle)$. For an odd number of ions the produced state is still a maximally GHZ-class entangled state which can be transferred to a GHZ state by an additional collective local operation $R_\phi(\pi/2)$.

Implementing the MS gate requires the application of a bichromatic light field $E(t) = E_+(t) + E_-(t)$ with constituents $E_\pm = E_0 \cos((\omega_0 \pm (\omega_z + \delta))t)$ where ω_0 is the qubit transition frequency, ω_z denotes the frequency of the motional mode and δ is an additional detuning. The level scheme of the MS operation acting on a two-ion register is shown in figure 3b). Mølmer and Sørensen showed that if the detuning from the sideband δ equals the coupling strength on the sideband $\eta\Omega$ the operation $MS(\pi/2)$ is performed when the light field is applied for a duration $t = 2\pi/\delta$.

However, implementing MS operations with rotation angles $\pi/2$ is not sufficient for universal quantum computation. Arbitrary rotation angles θ can be implemented with the same detuning δ by adjusting the Rabi frequency on the motional sideband to $\eta\Omega = \delta \sqrt{\theta/(\pi/2)}$. Due to this fixed relation between the rotation angle and the detuning, the gate operation needs to be optimized for each value of θ . In practice this optimization is a time-consuming task and thus the gate is optimized only for the smallest occurring angle in the desired algorithm. Gate operations with larger rotation angles are realized by a concatenation of multiple instances of the already optimized operation.

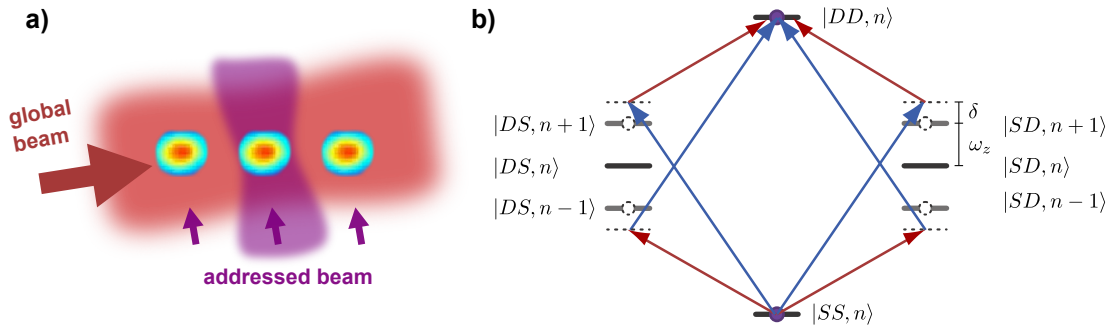


Figure 3. a) Schematic view of the laser beam geometry for qubit manipulation. b) Schematic level scheme of a Mølmer Sørensen type interaction. The bichromatic light field couples the states $|SS, n\rangle$ with $|DD, n\rangle$ via the intermediate states $|SD, n \pm 1\rangle$ and $|DS, n \pm 1\rangle$ with a detuning δ .

If the physical system consisted of a two-level atom coupled to a harmonic oscillator the AC-Stark introduced by one off-resonant light field would be perfectly compensated by its counterpart in the bichromatic field. However, $^{40}\text{Ca}^+$ shows a rich level structure where due to the additional Zeeman levels and coupling to the other $4P$ states an additional AC-Stark shift is introduced [22]. This shift changes the transition frequency between the two qubit states which has the effect that the detuning from the sideband transition δ is not equal for both constituents of the bichromatic light field. This would degrade the quality of the operation drastically and thus the shift has to be compensated which can be achieved by two distinct techniques [23]: (i) The center frequency of the bichromatic light field can be shifted or (ii) the light intensity of the two constituents can be unbalanced to induce a Stark shift on the carrier transition which compensates the unwanted Stark shift. Depending on the application, one compensation method is preferable over the other. Method (i) makes it easier to optimize the physical parameters to achieve very high gate fidelities but leads to an additional global rotation around σ_z which

is tedious to measure and compensate for in a complex algorithm. This can be avoided by method (ii) but the compensation is not independent of the motional state leading to a slightly worse performance [23]. Therefore, we generally choose method (i) if the goal is to solely generate a GHZ state whereas method (ii) is favorable if the gate is part of a complex algorithm.

In general an algorithm requires operations with positive and negative values of the rotation angles for the available operations. For the resonant $R_\phi(\theta)$ operation both signs of θ can be realized by changing the phase of the light field since $e^{-i(-\theta)S_\phi} = e^{-i\theta S_{(\pi+\phi)}}$ which is not possible for MS operations as $S_\phi^2 = S_{\phi+\pi}^2$. The sign of the rotation of the MS operation angle can only be adjusted by choosing the sign of the detuning δ [24]. However, performing MS operations with positive and negative detunings results in a more complex setup for generating the required RF signals and also a considerable overhead in calibrating the operation. Therefore it can be favorable to implement negative θ by performing $MS_\phi(\pi - |\theta|)$ which works for any odd number of ions whereas for an even number of ions, an additional $R_\phi(\pi)$ operation is required [24]. With this approach the quality of operations with negative rotation angles is reduced but the experimental overhead is avoided.

1.4. Optimized sequences of operations

Typically, quantum algorithms are formulated as quantum circuits where the algorithm is build up from the standard set of operations containing single qubit operations and CNOT gates. Implementing such an algorithm is straightforward if the implementation can perform these standard gate operations efficiently. Our set of gates is universal and thus it is possible to build up single qubit and CNOT operations from these gates. However, it might be favorable to decompose the desired algorithm directly into gates from our implementable set as the required sequence of operations might require less resources. This becomes evident when one investigates the operations necessary to generate a four-qubit GHZ state. Here, a single MS gate is able to replace four CNOT gates.

The problem of breaking down an algorithm into an optimized sequence of given gate operations was first solved by the NMR quantum computing community. There, a numerical optimal control algorithm was employed to find the sequence of gate operations that is expected to yield the lowest error rate for a given unitary operation [25]. This algorithm optimizes the coupling strength of the individual parts of the Hamiltonian towards the desired sequence. Unfortunately the NMR algorithm is not directly applicable to our ion trap system as the set of operations differ. In an NMR system the interactions are present at all times, only their respective strengths can be controlled. This allows for an efficient optimization as there is no time order of the individual operations. This is not true for current ion trap quantum computers where only a single operation is applied at a time which makes it necessary to optimize the order of the operations within the sequence in addition to the rotation angles. Furthermore, the same type of operation might appear several times at different positions. Thus we modified the algorithm so that it starts from a long random initial sequence and optimizes the rotation angles of the operation. This optimization converges towards the desired algorithm, if the required sequence is a subset of this random initial sequence. The key idea of our modification is that rotation angles of operations that are included in the random initial sequence but are not required for the final sequence shrinks during the optimization. If the rotation angle of an operation shrinks below a threshold value, the operation is removed from the

sequence as it is superfluous. If the algorithm fails to find a matching sequence, further random operations are inserted into the sequence. A more detailed treatment on the algorithm is given in reference [26]. In general this optimization method is not scalable as the search space increases exponentially with the number of qubits but it is possible to build up an algorithm from optimized gate primitives acting on a few qubits.

Even for complex algorithms on a few qubits, the sequence generated with this optimization method might include too many operations to yield acceptable fidelities when implemented. Then it can be advantageous to split the algorithm in parts that act only on a subset of the register and generate optimized decompositions for these parts. For this task, the physical interactions need to be altered so that they only affect the relevant subset. Multiple techniques for achieving this in ion traps have been proposed, where the best known techniques rely on physically moving and splitting the ion-chains in a complex and miniaturized ion trap [27]. Our approach to this problem is to decouple them spectroscopically by transferring the information of the idling ions into a subspace that does not couple to the resonant laser light. Candidates for such decoupled subspaces are either (i) $4S_{1/2}(m_j = +1/2)$ with $3D_{5/2}(m_j = +1/2)$ or alternatively (ii) $3D_{5/2}(m_j = -5/2) = |D'\rangle$ with $3D_{5/2}(m_j = -3/2) = |D''\rangle$. The decoupling technique (ii) is sketched in figure 4a). The only remaining action of the manipulation laser on the decoupled qubits is then an AC-Stark shift that acts as a deterministic rotation around the Z-axis. This rotation can be measured and subsequently be compensated for by controlling the phase of the transfer light. When qubits in the set U are decoupled, the action of the operations can then be described by $(\prod_{j \in U} 1_j) \otimes U$ where the operation U is the implemented interaction on the desired subspace. Note that the parameters of the MS operations do not change when the number of decoupled qubits is altered thus the gate does not need to be re-optimized.

1.5. Tools beyond coherent operations

In general, any quantum computer requires non-reversible and therefore also non-coherent operations for state initialization and measurements [18]. For example, quantum error correction protocols rely on controlled non-coherent operations within an algorithm to remove information on the error from the system similar to state initialization. Furthermore, the robustness of a quantum state against noise can be analyzed by exposing it to a well defined amount of phase or amplitude damping [28]. Surprisingly, it has been shown theoretically that non-coherent operations can serve as a resource for quantum information [24, 29, 30]. Naturally, these ideas can only be implemented if controlled non-coherent operations are available in the system. Mathematically, these non-reversible operations are described by a trace-preserving completely positive map $\mathcal{E}(\rho)$ acting on a density matrix rather than unitary operations acting on pure states. The action of such a map is described by $\mathcal{E}(\rho) = \sum_k E_k^\dagger \rho E_k$ with Kraus operators E_k fulfilling $\sum_k E_k^\dagger E_k = 1$ [18].

In our system two different variations of these controlled dissipative processes are available [31]: The archetype of a controlled non-coherent optical process is optical pumping. We can perform optical pumping on individual qubits inside the register with the following sequence as shown in figure 4c): (i) Partially transfer the population from $|D\rangle$ to $|S'\rangle$ with probability γ , and (ii) optical pumping from $|S'\rangle$ to $|S\rangle$ analogous to the qubit initialization. The partial population transfer is performed by a coherent

rotation with an angle θ on the transition $4S_{1/2}(m_j = +1/2) \leftrightarrow 3D_{5/2}(m_j = -1/2)$ which leads to $\gamma = \sin^2(\theta)$. This reset process can be described as controlled amplitude damping on an individual qubit where the map affecting the qubit is shown in table 1. Note that the information in the qubit states is not affected as the optical pumping light couples to neither of the original qubit states. For a full population transfer ($\gamma = 1$) the procedure acts as a deterministic reinitialization of an individual qubit inside a register as required for repetitive quantum error correction [32].

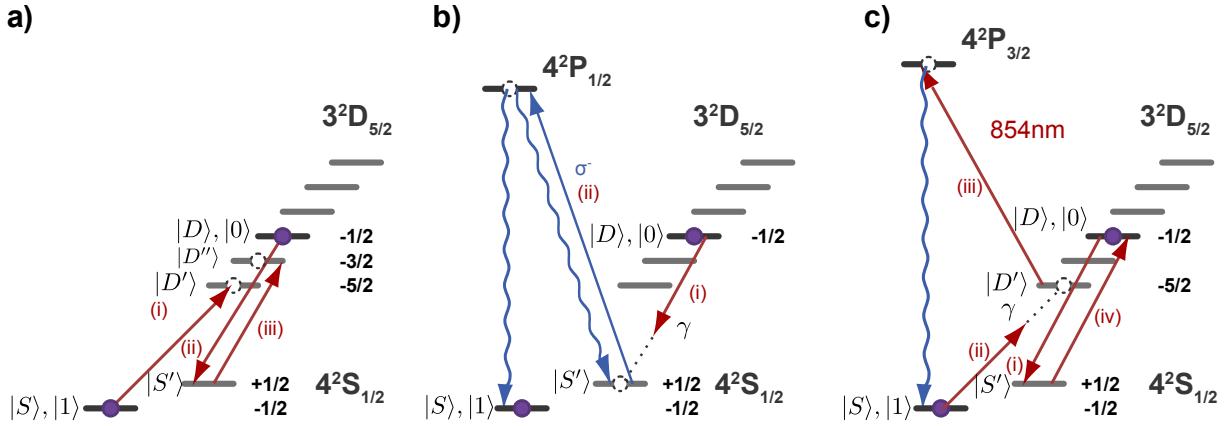


Figure 4. a) The process to decouple individual qubits: (i) The population from $|S\rangle$ is transferred to $|D'\rangle$. (ii) The population from $|D\rangle$ is transferred to $|S'\rangle$ and subsequently to (iii) $|D''\rangle$. b) Implementing controlled amplitude damping using the 397nm σ beam. (i) Transferring the population from $|D\rangle$ to $|S'\rangle$. (ii) Optical pumping of $|S'\rangle$ using light at 397nm. c) Controlled phase damping with strength γ utilizing light at 854nm. (i) Population from $|D\rangle$ is hidden in the $|S'\rangle$ state. (ii) The population from $|S\rangle$ is partially brought to $|D'\rangle$ and (iii) shining in light at 854 nm depletes the $3D_{5/2}$ via $4P_{3/2}$ and finally (iv) the population is brought from $|S'\rangle$ back to $|D\rangle$.

Furthermore an alternative implementation of optical pumping can be used to generate controlled phase damping. This process preserves the populations in the respective qubit states but destroys the coherences between them with probability γ : (i) The information residing in state $|D\rangle$ of all qubits is protected by transferring it to the $|S'\rangle = 4S_{1/2}(m_j = +1/2)$ state before the reset step. (ii) On the qubit to be damped, the population from $|S\rangle$ is partially transferred into the $|D'\rangle = 3D_{5/2}(m_j = -5/2)$ state with probability γ . Here, the partial population transfer is performed by a coherent rotation on the transition $4S_{1/2}(m_j = -1/2) \leftrightarrow 3D_{5/2}(m_j = -5/2)$ (iii) Shining light resonant with the $3D_{5/2} \leftrightarrow 4P_{3/2}$ transition at 854 nm onto the ions depletes this level to $|S\rangle$. (iv) Transferring $|S'\rangle$ back to $|D\rangle$ restores the initial populations, the coherence of the qubit has been destroyed with probability γ . The schematic of this process is shown in figure 4b) and the resulting map can be found in table 1.

Our system furthermore allows the measurement of a single qubit without affecting the other qubits in the same ion string. For this, all spectator ions need to be decoupled from the detection light. This is realized by transferring the population from the $|S\rangle$ state to the $|D'\rangle = 3D_{5/2}(m_j = -5/2)$ state. Applying light on the detection transition measures the state of the ion of interest while preserving the quantum information encoded in the hidden qubits. This information can be used to perform conditional quantum operations as needed for teleportation experiments [17] or quantum non-demolition measurements [33].

It should be noted, that the operations forming our implementable set of gates shown in table 1 allow

the realization of any completely positive map, which corresponds to a Markovian process [33–35]. The quality of the operations is affected by multiple physical parameters that are discussed in more detail in section 3. In order to faithfully estimate the resulting fidelity of an implemented algorithm, a complete numerical simulation of the physical system has to be performed. However, a crude estimation can be performed assuming a fidelity of 99.5% for non-entangling operations and $\{98, 97, 95, 93, 90\}\%$ for the MS operations on a string of $\{2, 3, 4, 5, 6\}$ ions [36]. The fidelity of the entire algorithm is then estimated by simply multiplying the fidelities of the required operations.

Table 1. The extended set of operations in our ion trap QC. This set of operations allows us to implement any possible Markovian process.

Name	Addressed/global	Ideal operation
AC-Stark shift pulses	addressed	$S_z^{(i)}(\theta) = e^{-i\theta/2\sigma_z^{(i)}}$
Collective resonant operations	collective non-entangling	$S_\phi(\theta) = e^{-i\theta/2S_\phi}$
Mølmer-Sørensen	collective entangling	$MS_\phi(\theta) = e^{-i\theta/2S_\phi^2}$
Phase damping	addressed non-coherent	$E_0^p = \begin{vmatrix} 1 & 0 \\ 0 & \sqrt{1-\gamma} \end{vmatrix} \quad E_1^p = \begin{vmatrix} 0 & 0 \\ 0 & \sqrt{\gamma} \end{vmatrix}$
Amplitude damping	addressed non-coherent	$E_0^a = \begin{vmatrix} 1 & 0 \\ 0 & \sqrt{1-\gamma} \end{vmatrix} \quad E_1^a = \begin{vmatrix} 0 & \sqrt{\gamma} \\ 0 & 0 \end{vmatrix}$
Single-qubit measurement	addressed non-coherent	Projection onto $ 0\rangle\langle 0 $ or $ 1\rangle\langle 1 $

2. Experimental setup

In this section we give an overview of the experimental setup of our ion-trap quantum information processor. First, we describe in detail the ion trap, the optical setup and the laser sources. Then we concentrate on the experiment control system and techniques to infer the state of the qubit register.

2.1. The linear Paul trap

The trap in our experimental system is a macroscopic linear Paul trap with dimensions as shown in figure 5 [11]. The trap is usually operated at a radial motional frequency of 3MHz and an axial motional frequency of 1MHz. These trapping parameters are slightly adjusted with respect to the number of ions in the string to prevent overlap of the frequencies from different motional modes of all transitions. In order to minimize magnetic field fluctuations, the apparatus is enclosed in a magnetic shield (75x75x125 cm) that attenuates the amplitude of an external magnetic field at frequencies of above 20 Hz by more than 50dB ‡. The trap exhibits heating rates of 70ms per phonon at an axial trap frequency of 1MHz. Micromotion of a single ion can be compensated with the aid of two compensation electrodes. The remaining micromotion creates sidebands at the trap frequency which can be observed in an ion spectrum on the qubit transition. The strength of the excess micromotion is described by the modulation index β of these sidebands where in our setup a modulation index of $\beta < 1\%$ is observed [37, 38].

‡ Imedco, Proj.Nr.: 3310.68

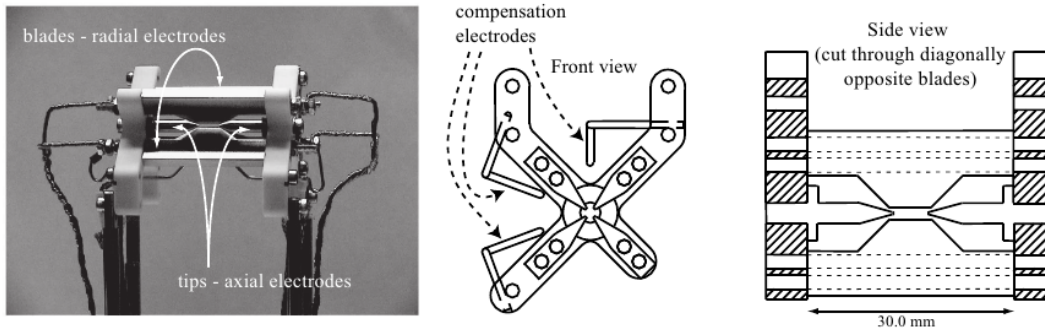


Figure 5. Schematic drawing of the linear Paul trap used in our experiment. The distance between the endcaps is 5mm whereas the distance between the radio-frequency blades is 1.6mm.

2.2. Optical setup

A quantum information processor with $^{40}\text{Ca}^+$ requires multiple laser sources, listed in table 2, to prepare, manipulate and measure the quantum state of the ions. The ions are generated from a neutral atom beam with a two-step photo-ionization process requiring laser sources at 422nm and 375nm. Manipulating the state of the qubits is done with a Titanium-Sapphire laser at 729nm on the $4S_{1/2} \leftrightarrow 3D_{5/2}$ qubit transition and its setup as described in reference [39]. Its frequency and amplitude fluctuations affect crucially the performance of the coherent operations as will be discussed in section 3. The laser has a linewidth of below 20Hz and the relative intensity fluctuations are in the range of 1.5% [39].

Transition	Wavelength	Usage	Linewidth
$4S_{1/2} \leftrightarrow 4P_{1/2}$	397nm	Doppler cooling, optical pumping and detection	<1MHz
$4S_{1/2} \leftrightarrow 3D_{5/2}$	729nm	Sideband cooling and qubit manipulation	< 20Hz
$3D_{3/2} \leftrightarrow 4P_{1/2}$	866nm	Repumping for detection	<1MHz
$3D_{5/2} \leftrightarrow 4P_{3/2}$	854nm	Quenching for Sideband cooling and qubit reset	<1MHz
neutral calcium	422nm	Photoionization first stage	-
neutral calcium	375nm	Photoionization second stage	-

Table 2. Laser wavelengths needed for a Ca^+ ion trap experiment. The lasers are stabilized to a reference cavity with the Pound-Drever-Hall locking technique except for the photoionization lasers which are not actively stabilized.

The vacuum vessel housing the trap and the laser sources reside on different optical tables and thus the light is transferred between different tables with optical fibers. The optical access to the trap itself is constrained by the surrounding octagon vacuum vessel which is sketched in figure 6 including the available beams with their respective directions. The 397nm light is required for multiple tasks and thus multiple beams are required: one beam for Doppler cooling and detection, another beam for optical pumping (labeled Pumping σ), and two beams for Raman sideband-cooling (labeled Raman σ , Raman π). In particular, the beams used for optical pumping need to be aligned with the magnetic field generated by

the coils as indicated in figure 6. In practice it is favorable to adjust the orientation of the magnetic field with respect to the light beam since the magnetic field can be adjusted without moving any mechanical part. The beams of the 866nm and 854nm laser are overlapped with the 397nm detection beam in a single-mode photonic crystal fiber.

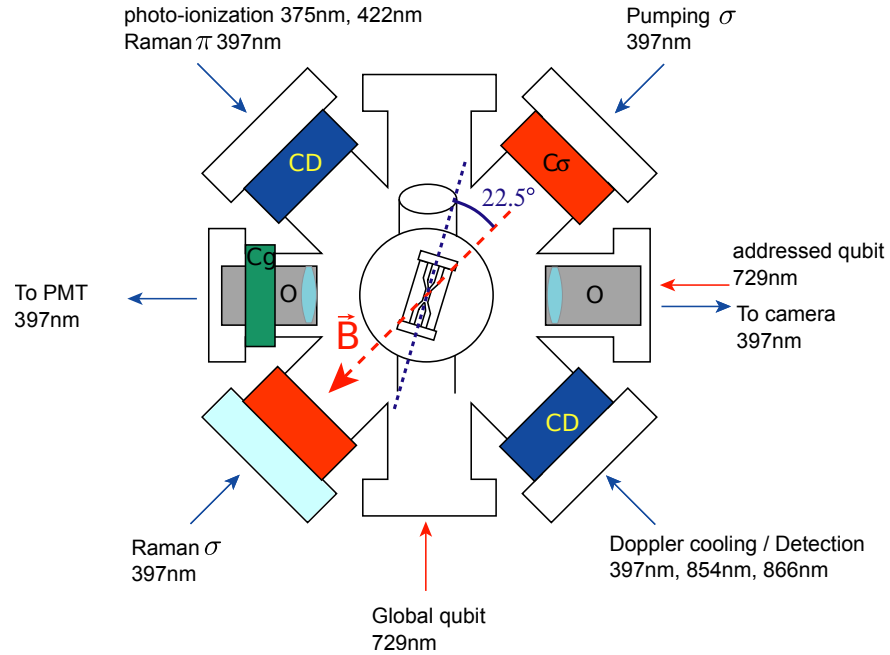


Figure 6. Overview of the alignment of the various laser beams, the coils generating the magnetic field and the trap with respect to the vacuum vessel.

In order to implement our set of operations, the 729 nm light needs to be applied to the ions from two different optical ports: (i) the addressed beam which is a tightly focused beam illuminating only a single ion and (ii) the global beam which is a wide beam that illuminates all ions with an approximately homogeneous light intensity. The angle between the global beam and the axial trap axis is 22.5° which leads to a Lamb-Dicke parameter of $\eta_{glob} = 6\%$ [40]. The width of the beam is chosen so that the light intensity shows variations of less than 2% over the entire ion string. Considering that the ions are arranged in a linear crystal, it is advantageous to use an elliptical shape for the global beam to achieve higher light intensities at the position of the ions. The elongated axis of the beam has typically a diameter of $100\mu m$ which is sufficient for ion strings with up to 8 ions. For larger ion strings, the beam size needs to be enlarged which increases the required time for performing collective operations.

The angle between the addressed beam and the trap axis is 67.5° which results in a smaller Lamb-Dicke parameter of $\eta_{add} = 2.5\%$. The addressed beam needs to be able to resolve the individual ions in the string which means that the beam size needs to be smaller than the inter-ion distance of approximately $5\mu m$. This small beam size is realized with the aid of a custom high numerical aperture objective situated in an inverted viewport as sketched in figure 7a). Additionally, the beam has to be rapidly switched between the ions which is realized with an electro-optical deflector (EOD). The switching speed depends on the

capacitance of the EOD and the output impedance of the driving high voltage amplifier. Figure 7b) shows the voltage on the EOD during a switching event between two neighboring ions which demonstrated that a switching event requires approximately $15\mu s$. Experience has shown that a delay between the switching event and the next light pulse of $30\mu s$ is sufficient to switch between arbitrary ions in a string of up to 8 ions. Note that the voltage ramp measured at the EOD can only serve as an indicator for the position of the laser beam but does not provide information about the settling time of the laser light phase at the position of the ion. It was observed that the phase of the light field keeps changing for more than $100\mu s$ after a switching event. However, this does not affect the qubit operations for our set of operations as the AC-Stark shift does not depend on the phase of the light field as described in section 1.

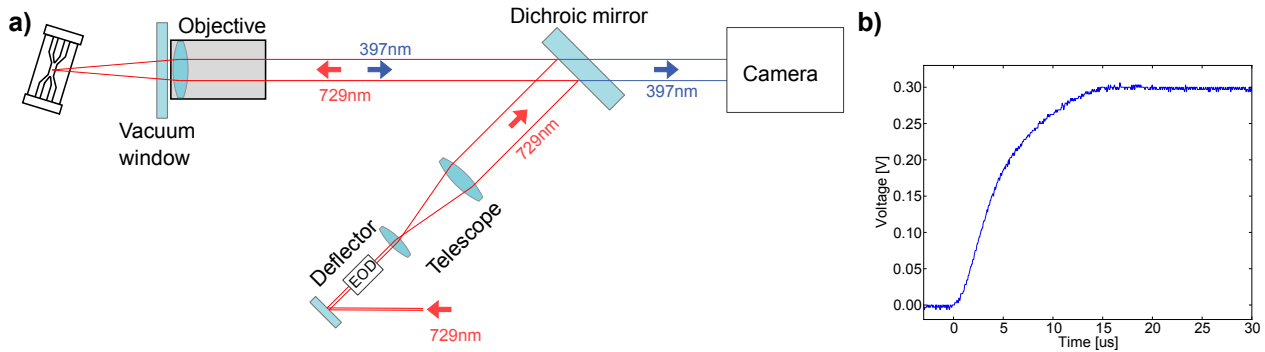


Figure 7. a) Optical setup for the addressing beam setup. b) Time dependence of the voltage on the EOD switching between two neighboring ions. After approximately $15\mu s$ the voltage settles and thus the switching process is finished.

2.3. Experiment control

Any ion-trap quantum information experiment requires precise and agile control of duration, frequency and amplitude of laser beams originating from multiple sources. A typical experimental sequence consists of optical pumping, cooling the center-of-mass (COM) mode, coherent operations and qubit measurements as shown in figure 8a). Usually the required control is achieved by using acousto-optical devices which map the control over intensity and frequency of the light field onto the manipulation of amplitude and frequency of a radio-frequency (RF) signal. Thus, versatile and fast radio-frequency (RF) signal generators are a necessity for a high-fidelity quantum information processor. Modern RF signal generators are commonly based on direct digital synthesizers (DDS) enabling switching times on a nanosecond timescale and frequencies between 1 and 400 MHz with sub-Hertz resolution. In our experiment, these DDSs are controlled by a special purpose microcontroller embedded on a field-programmable-gate-array (FPGA) [41]§. This FPGA is able to generate digital pulses with a duration from 10ns up to several seconds. In order to allow coherent rotation on different transitions to be realized, the control system needs to be able to perform phase-coherent switching between multiple frequencies. The phase stability of the phase-coherent switching has been tested to be $0.0001(90)^\circ$ [38]. The controller is connected to the experimental control computer via a standard ethernet connection. For quantum algorithms requiring feed-forward operations, such as teleportation, it is necessary to use the outcome

§ <http://pulse-programmer.org>

of a measurement within the algorithm to control subsequent operations in the algorithm. This can be realized by analyzing the measurement outcome by counting the PMT signal on dedicated counters and performing the controlled operations in the sequence depending on state of this counters [17]. A schematic view of the control system including this feedback mechanism is shown in figure 8b).

Parameter	Type	Required for each ion
Ion position	Voltage	yes
Telescope lens position	Position	no
Rabi frequency	Time	yes
Zeeman splitting	Magnetic field	no
Laser frequency drift	Frequency	no

Table 3. List of automatically calibrated parameters.

The FPGA determining the timing of the experiment is itself controlled by a personal computer running a custom LabView program. This program translates the sequence of operations from a human readable format to binary code that can be executed on the FPGA. In order to minimize the required time for calibrating the system, the parameters shown in table 3 are calibrated automatically without any user input. Our set of operations can only be implemented, if the frequency of the manipulation laser is close to the qubit transition frequency. Since the frequency of each individual transition is mainly determined by the center frequency of all transitions shifted by the respective Zeeman shift due to the applied magnetic field, it is sufficient to infer the magnitude of the magnetic field and the frequency difference between the laser and the center frequency. For this, the difference frequencies between the laser and two distinct transitions are measured on the transitions $4S_{1/2}(m_j = -1/2) \leftrightarrow 3D_{5/2}(m_f = -1/2)$ and $4S_{1/2}(m_j = -1/2) \leftrightarrow 3D_{5/2}(m_f = -5/2)$ which allows us to determine the long-term drift of the magnetic field and the 729 nm reference cavity. Typical values for the magnetic field drift are $10^{-8} G/s$ and for the cavity drift 60 mHz/s which is expected due to aging of the cavity spacer crystal [42].

In order to perform addressed single-qubit operations, the position of the addressed beam with respect to the ion positions needs to be characterized. The position of the beam is controlled via the motorized lens before the objective, as indicated in figure 7a), and the voltage that is applied to the EOD. The calibration routine consists of moving the beam onto the center of the ion string with the motorized lens, followed by finding the EOD voltages for every individual ion. The position of the beam with respect to the ions can be determined to approximately 50nm. In order to perform the desired operations, the Rabi oscillation frequencies on the global beam and the addressed beam need to be measured. On the global beam, the Rabi frequencies of the two transitions required for the drift compensation need to be calibrated, whereas on the the addressed beam, the oscillation frequencies for each ion for the AC-Stark operations are measured using Ramsey spectroscopy. In general, the frequencies can be determined with a precision of approximately 1%.

2.4. Measuring individual ions within a quantum register

As described in section 1, measuring the quantum state of the ions is performed by counting single photons on the $4S_{1/2} \leftrightarrow 4P_{1/2}$ transition. We use high numerical aperture objectives located in an

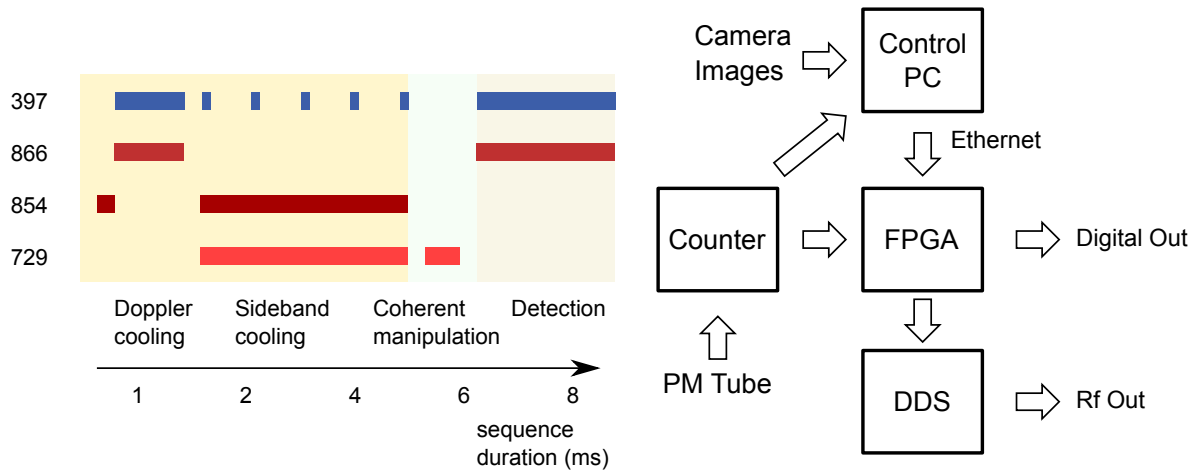


Figure 8. a) Timing sequence of the different lasers for a typical experiment consisting of state initialization, coherent manipulation and measurement. b) Schematic representation of the experiment control hardware. The FPGA is programmed by the experimental control PC and controls the timing of all signals used in the experiment. RF signals for the coherent manipulation are generated by DDS. It is possible to perform conditional operations based on measurement outcomes with external counters that analyze the photon counts from the PMT.

inverted viewport to reduce the distance between the ion and the objective as shown in figure 6. Two detection channels are available: one with a photo-multiplier-tube (PMT) and another with an electron multiplying CCD camera. The PMT integrates the photons over its sensitive area and thus cannot infer any spatial information on the ions. The number of detected photon counts depends on the number of bright ions as is indicated in the histogram of PMT counts shown in figure 9. By setting appropriate thresholds it is then possible to determine the number of ions found in the $4S_{1/2} = |0\rangle$ state which is sufficient information for performing permutationally invariant state tomography [43] or determining the fidelity of a multi-qubit GHZ state [36].

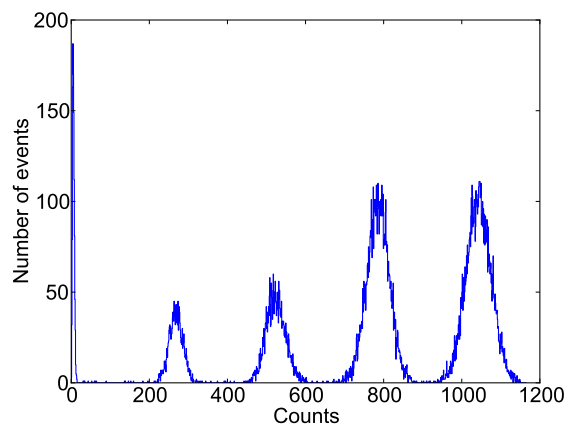


Figure 9. Histogram of counted pulses from the PMT for a 4 ion string. The histogram is derived from 21200 measurements with a detection time of 5ms.

In contrast, the CCD camera provides spatially resolved information of the detected light and is thus able to determine the state of each ion in the string separately. For fluorescence detection, the same objective

is used as for the focused 729nm beam is used. As sketched in figure 7a), the light at 729nm and at 397nm are separated by a dichroic mirror. The analysis of the camera data is performed in five steps: (i) A camera image is taken with an exposure time of 7ms. The value of each pixel corresponds to the number of detected photons. (ii) For further analysis, a limited region of interest (ROI) around the ion's position of the whole camera image is used. For a register of 4 ions the ROI consists of 35x5 pixels but the ROI size needs to be adjusted to the length of the ion string. (iii) The pixel values are summed over the y-axis of the ROI-image to get the brightness information along the ion string. (iv) This brightness distribution is then compared to pre-calculated distributions which are generated from a reference image where all ions are bright. From this reference image, the position and brightness distribution of each ion are determined. The state of the ion string is then inferred by comparing the summed pixel values with the pre-calculated distributions of each possible outcome by calculating the mean squared error χ^2 . Finally, (v) the state with the smallest mean squared error is chosen to be the most likely state. Two examples of this analysis procedure are shown in figure 10. Note that this method is not scalable as the number of pre-calculated distributions grows exponentially with the number of ions. However recent work on state detection in trapped ion system promises efficient detection schemes [44].

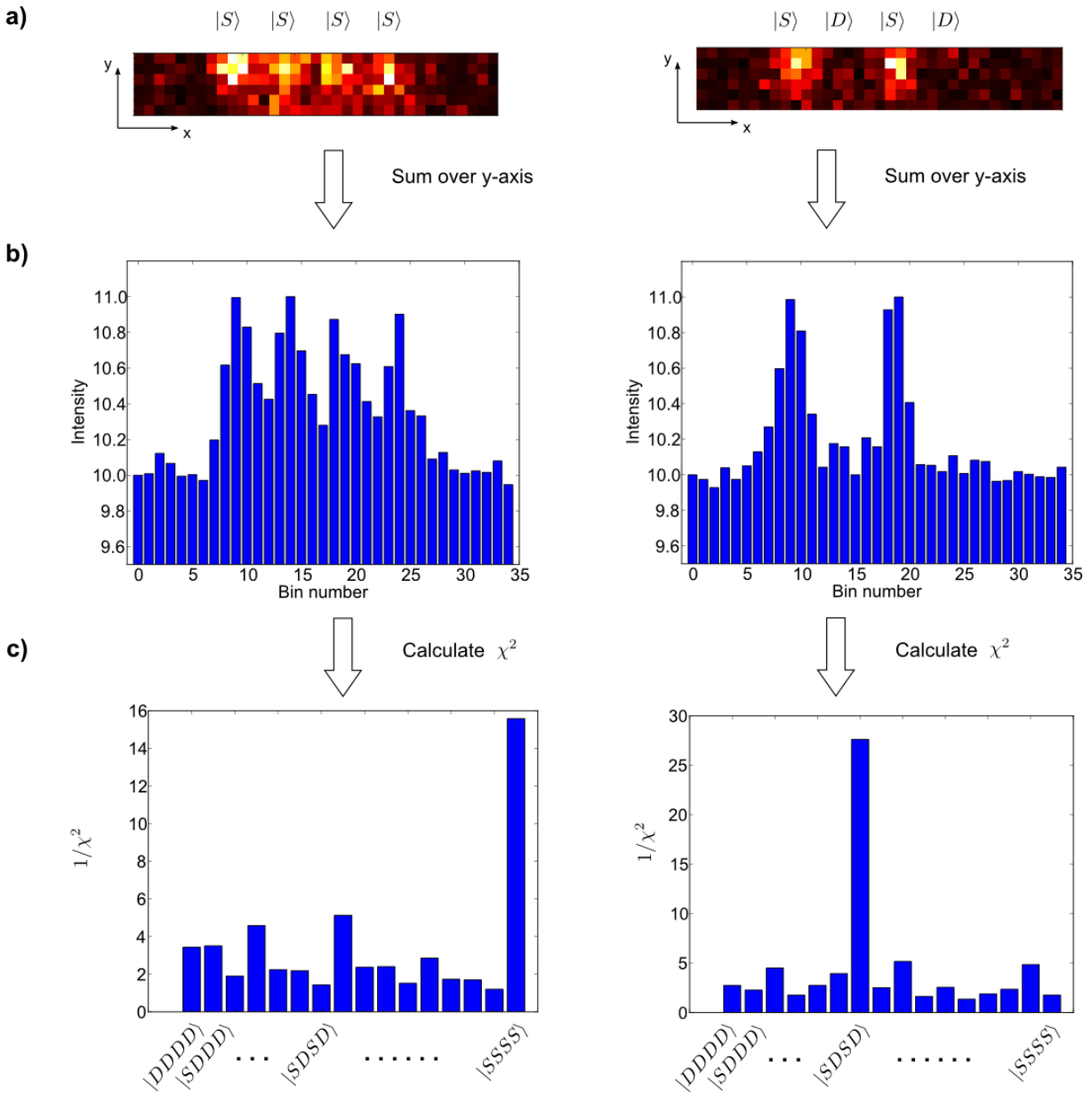


Figure 10. Schematic illustration of the camera detection in a 4 ion register. (a) False color image of the region of interest. (b) Brightness information after summation over the y-axis of the image. (c) $1/\chi^2$ of the sum with generated data for every possible state. The peak corresponds to the most likely state. In this case index 6 (15), which corresponds to the state $|SDSD\rangle$ ($|SSSS\rangle$), is the most likely state.

3. Error sources

Any implementation of a quantum computer will be affected by errors which ultimately need to be corrected with quantum error correction techniques. Identifying and characterizing the noise sources are therefore crucial steps towards a large-scale quantum information processor. In this analysis we distinguish noise sources, that affect a qubit used as a quantum memory, from additional error sources, that occur when performing operations. For the presented error sources, we describe the origin, present a method to characterize the magnitude, and provide typical values for our experimental system.

3.1. Errors in the qubit memory

In general, errors affecting a qubit memory are described by a combination of phase damping and amplitude damping [18]. In optical qubits, amplitude damping corresponds to decay from the excited to the ground state whereas phase damping destroys the phase of a superposition state but does not alter the population of the qubit. The lifetime of the excited qubit is a fundamental property of the ion species and gives an upper limit to the storage time of a quantum memory encoded in an optical qubit. In the experiment, the lifetime of the excited state can be reduced due to residual light fields depleting the $3D_{5/2}$ state via another state, or by collisions with background gas particles. This possible error source can be investigated by confirming that the time constant of the exponential decay from the $3D_{5/2}$ state is close to the natural lifetime of 1.168(7)s [45]. In our setup, we find a lifetime of $\tau_1 = 1.13(5)s$ [31].

The second noise type, phase damping, is usually investigated with Ramsey spectroscopy which determines the coherence properties of a superposition state [11]. There, the qubit is initially prepared in an equal superposition of the two computational states by a $R_0(\pi/2)$ rotation. After a certain storage time, a second rotation $R_\pi(\pi/2)$ is applied that ideally maps the qubit back into the state $|1\rangle$. If the phase ϕ of the second pulse $R_\phi(\pi/2)$ is varied with respect to the first pulse, the probability of being in state $|1\rangle$ is a periodic function of ϕ . If the coherence of the state is decreased due to phase damping, the second mapping pulse cannot reach the basis states anymore which is observed as a decrease in the amplitude of the oscillation. This loss of contrast corresponds directly to the remaining phase coherence of the superposition which naturally decreases with increasing storage time.

In our system, phase damping is predominantly caused by fluctuations between the frequency of the qubit transition and the driving field. The two main contributions are (i) laser frequency fluctuations and (ii) fluctuations in the magnetic field which cause fluctuations of the qubit transition frequency. It is then possible to distinguish between these contributions by investigating the coherence decay on multiple transitions between different Zeeman substates of the $4S_{1/2}$ and $3D_{5/2}$ levels because they show different susceptibility to the magnetic field due to different Lande g-factors. In figure 11a) the blue rectangles represent the coherence decay on the $4S_{1/2}(m_j = -1/2) \leftrightarrow 3D_{5/2}(m_j = -1/2)$ transition which is least sensitive to fluctuations in the magnetic field. The green diamonds show the coherence decay for the $4S_{1/2}(m_j = -1/2) \leftrightarrow 3D_{5/2}(m_j = -5/2)$ which has approximately 5 times higher sensitivity to fluctuations of the magnetic field [38, 46]. Note that both transitions show effectively the same coherence decay for storage times up to 1ms. This suggests that for typical experiments where the coherent manipulation is shorter than 1ms, the main source for dephasing are laser-frequency fluctuations.

The phase damping process can be theoretically described by a model that applies random phase flips with a certain probability p to multiple copies of the same state. The ensemble of all states is then described by a density matrix whose off-diagonal elements are affected by the phase damping as $\rho_{i,j} \xrightarrow{i \neq j} \rho_{i,j}(1 - 2p)$. This model of a phase-flip rate is close to the concept of a bit-flip rate used in classical computer science and is therefore widely used in theoretical works on quantum information [18]. However, a physical model for phase damping describes the phase-flip probability as a function of the information storage time. In order to do so, one has to find a noise-model describing temporal correlations of the noise source. The most straightforward noise model assumes temporally uncorrelated noise which leads to an exponential decay of the coherence characterized by the transversal coherence time τ_2 and therefore

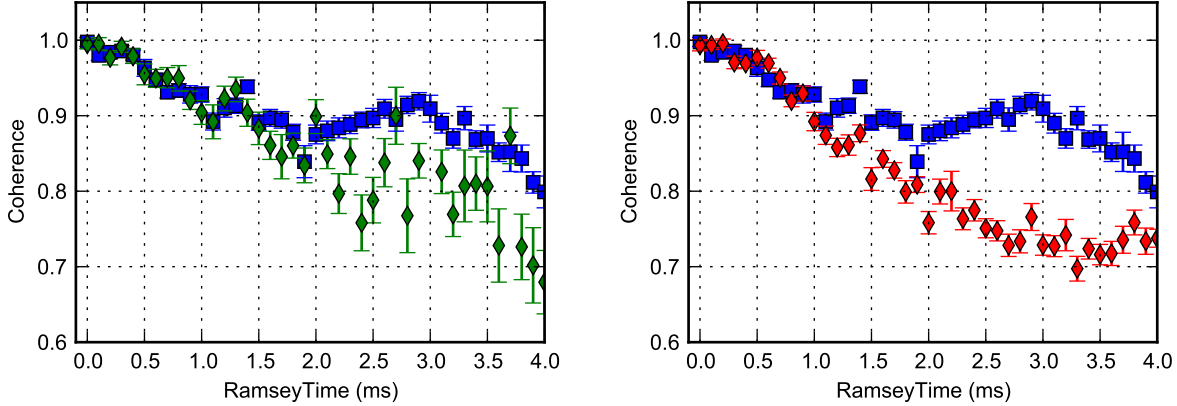


Figure 11. a) Ramsey contrast decay on two transitions with different sensitivity to the magnetic field fluctuations. Blue squares indicate the less sensitive $4S_{1/2}(m_j = -1/2) \leftrightarrow 3D_{5/2}(m_j = -1/2)$ transition whereas green diamonds correspond to the $4S_{1/2}(m_j = -1/2) \leftrightarrow 3D_{5/2}(m_j = -5/2)$ transition. b) Ramsey contrast decay on the transition which is least sensitive to magnetic field fluctuations, without (blue squares) and with (red diamonds) spin echo.

to off-diagonal elements $\rho_{i,j} = \rho_{i,j} e^{-t/\tau_2}$ [9]. This description is used in most quantum computing models where the noise can be fully characterized by the amplitude damping timescale τ_1 and the phase coherence time τ_2 [18]. In most physical systems, technical noise is temporally correlated and thus this simple model of uncorrelated phase noise does not apply [36]. In particular the coherence decay in our system deviates notably from an exponential decay as can be seen in figure 11a). This effect can be amplified with the aid of a well known method to enhance the storage time of a quantum memory known as the spin-echo technique. There, the basis states are swapped at half the storage time which reverses the phase evolution and thus cancels fluctuations provided their timescale is longer than the storage time. However, it is possible that the performance with a single echo is worse than the original register if this condition is not satisfied. This effect is demonstrated in figure 11b) where the coherence with spin-echo (red diamonds) is worse than without echo (blue squares). There exist more sophisticated methods to enhance the qubit storage time which are able to take temporal correlations into account. A formal description of this techniques is known as dynamical decoupling which has already been demonstrated in various physical systems [47–53]. For a given noise spectrum an optimal pattern of echo pulses can be determined to maximize the phase coherence. Interestingly, one can use this technique to determine the spectral noise density from multiple coherence decays with varying number of echos [54, 55]. In the following we describe a simple experiment for identifying the dominant features of the noise spectrum without using any spin echo technique.

It is possible to infer the noise spectrum from a coherence decay $C(T)$ without any echo when only a few parameters of the noise spectrum need to be determined. For a given noise spectrum $A(\omega)$, the Ramsey contrast decay is given by

$$C(T) = \exp \left\{ - \int_0^\infty d\omega \frac{A(\omega)^2}{\omega^2} \sin^2(\omega T/2) \right\}.$$

which is a special case of the general coherence decay for dynamical decoupling given in reference [55]. Calculating the noise spectrum from a measured coherence decay is not uniquely possible, thus we

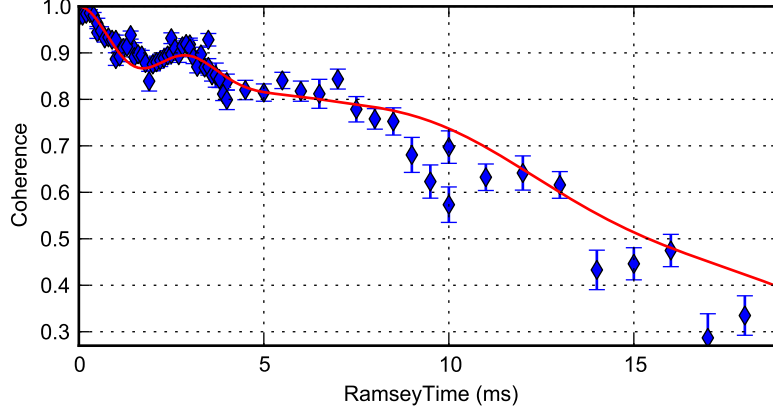


Figure 12. Measured Ramsey contrast decay on the $4S_{1/2}(m_j = -1/2) \leftrightarrow 3D_{5/2}(m_j = -1/2)$ transition. The solid line shows a modeled Ramsey contrast decay with fitted parameters.

characterize $A(\omega)$ assuming a certain spectral shape of the noise and inferring only a few parameters. Our main source of phase noise at relevant timescales smaller than 1ms seems to be the laser frequency noise and thus we model the spectrum accordingly. Typically a laser spectrum is modeled as a Lorentzian line, which we extend with two broad Gaussian peaks, where the first originates from the laser locking electronics centered at 300Hz and the second peak is attributed to the second harmonic of the power line frequency at 100Hz. We model these two contributions with Gaussian peaks $G_\nu(\omega) = \exp((\omega - \omega_0 - \nu)^2/\sigma^2)$ where $\sigma = 10\text{Hz}$. The resulting spectral noise density for our model is then

$$A(\omega) = \alpha \left(\frac{\gamma^2}{\gamma^2 + (\omega - \omega_0)^2} + a_1 G_{300}(\omega - \omega_0) + a_2 G_{100}(\omega - \omega_0) \right).$$

Noise at the fundamental frequency of the power line (50Hz) is not included in the model as it is not distinguishable from Gaussian noise for storage times below 10ms. Figure 12 shows the fitted coherence decay of the model with parameters $\alpha = 89\sqrt{\text{Hz}}$, $\gamma = 3\text{ Hz}$, $a_1 = 0.22$ and $a_2 = 0.02$.

When generalizing these results to multi-qubit systems, the spatial correlation of the noise on all qubits needs to be considered. In our system the noise from the laser and magnetic fields are almost identical over the entire register and therefore the phase noise can be modeled affecting the entire register simultaneously. This correlation leads to a faster loss of coherence between states with large total energy difference [36]. On the other hand, this spatial correlation enables decoherence free subspaces (DFS) which are not affected by dephasing. The DFS consists of states in which acquiring an equal phase on all qubits leads only to a global phase of the state and thus to no dephasing. For example, a single logical qubit can be encoded in two physical qubits as $|0_l\rangle = |01\rangle + |10\rangle$ and $|1_l\rangle = |01\rangle - |10\rangle$ respectively. The two logical states have identical total energy difference and thus form a DFS, where a universal set of operations with two logical qubits has been demonstrated in our system [56]. However, it is not clear how well the concept of a DFS can be extended to larger register sizes, and thus we show the coherence decay of an 8-qubit DFS state of the form $|00001111\rangle + e^{i\phi}|11110000\rangle$ in figure 13. The state is generated by preparing the qubit register in the state $|00001111\rangle$ and performing a $MS_{\phi=0}(\pi/2)$ operation. If the DFS is also present for 8 ions, the loss of coherence should correspond to the spontaneous decay of the $3D_{5/2}$ state resulting in an exponential decay of the coherence with timescale $\tau = \tau_1/n$ where $n = 4$

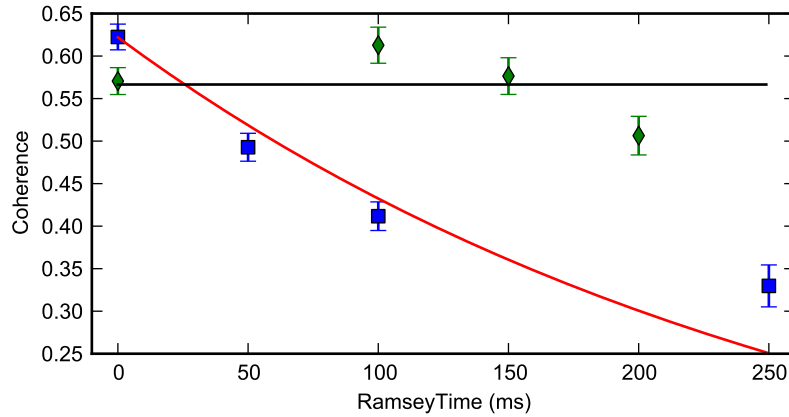


Figure 13. Coherence as a function of the qubit storage time of an 8-qubit DFS state encoded in the optical qubit (blue squares) and the ground-state qubit (green diamonds) eliminating amplitude damping decay. The solid lines represent the expected decay for both qubit types.

is the number of excited ions. This is illustrated in figure 13 showing the measured coherence decay and the expected decay, assuming only spontaneous decay. Furthermore, the spontaneous decay can be eliminated by encoding the qubit in the two substates of the $4S_{1/2}$ level as introduced in section 1. The red squares in figure 13 show no noticeable decay during a storage time of 200ms where limitations of the experiment control system (and PhD students) prevent investigating longer storage times. The storage time limit of this DFS is then given by fluctuations in the magnetic field gradient and is expected to be in the 30s regime [57].

3.2. Errors in quantum operations

Performing operations on the qubit adds additional noise sources, and thus the error rate of the entire algorithm cannot be described by spontaneous decay and phase damping. We will now describe these sources by their physical causes and categorize them by their occurrence in (i) state initialization, (ii) coherent manipulation and (iii) state detection.

3.2.1. Initialization As described in section 1 the qubit is initialized by means of an optical pumping process towards the $4S_{1/2}(m = -1/2)$ state using a circularly polarized laser beam aligned parallel to the magnetic field. The possible error sources are (i) imperfect polarization of the pumping light and (ii) misalignment with respect to the magnetic field. The polarization quality is determined by the quality of the polarization optics and the birefringence caused by stress on the window attached to the vacuum vessel. The quantization axis can be aligned by biasing the current in the different magnetic field coils. The error probability of this process can be measured by transferring the remaining population from the $4S_{1/2}(m = 1/2)$ to the $3D_{5/2}$ level and measuring it subsequently. If the transfer works perfectly, the population left in the $4S_{1/2}$ level is due to imperfect optical pumping. Since the transfer is imperfect, the population needs to be shelved multiple times to multiple substates in the $3D_{5/2}$ manifold. Every shelving pulse is performed with an error rate of less than 1% and thus the error rate of two combined shelving

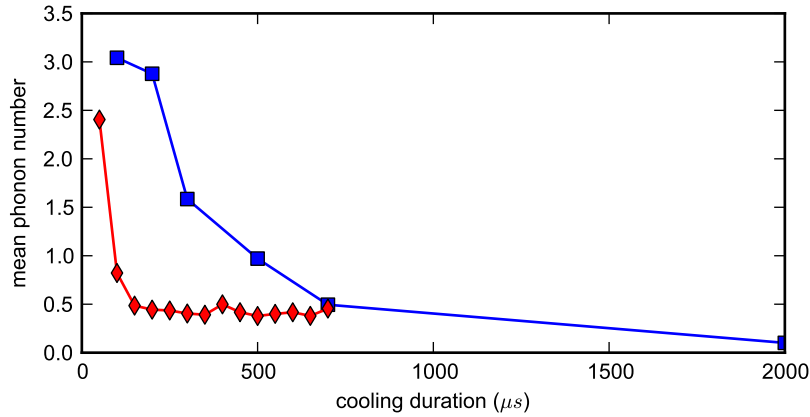


Figure 14. Cooling rates for sideband cooling on the Raman (red diamonds) and the optical (blue squares) transition. Although cooling via the Raman process is faster it leads to a higher steady state phonon number.

pulses is on the order of 10^{-4} . With this technique, the fidelity of the optical pumping process can be determined accurately. We find a fidelity of the optical pumping process of better than 99.1% [58]. The second optical pumping technique, as introduced in section 1, is frequency selective on the qubit transition. Thus the direction of the magnetic field with respect to the laser beam can be neglected which leads to a more robust pumping. With this technique we find a pumping fidelity of larger than 99% [59].

The second initialization step prepares the ion in the motional ground state of the harmonic oscillator. We treat the common-mode motion (COM) separate from the other modes as it is used by the entangling MS operations. In order to reach the lowest possible mean phonon number, sideband cooling on the qubit transition as described in section 1 is performed on the common mode after a Doppler pre-cooling cycle. The final phonon occupation can be determined by various techniques where a suitable method, when the motion is close to the ground state, is to perform Rabi oscillations on the motional sideband. This method uses the fact that the Rabi frequency on the blue sideband for a given phonon number n is given by $\Omega_n = \sqrt{n+1} \eta \Omega_0$ where Ω_0 is the Rabi frequency on the carrier transition. Rabi oscillations for a given phonon distribution are described by

$$p_{|1\rangle} = \sum_n c_n \sin^2(\eta \Omega_0 / 2 \sqrt{n+1} t)$$

where the parameters c_n can be determined by performing a numerical fit to the measured data assuming a thermal distribution of $c_n = \langle n \rangle^n / (\langle n \rangle + 1)^{n+1}$ which is completely described by the mean phonon number $\langle n \rangle$. A typical value for our experiments using sideband cooling on the optical transition is $\langle n \rangle = 0.05(3)$ after a cooling time of 2 ms [15]. In our setup we have also the possibility of performing sideband cooling on the Raman transition as introduced in section 1. This technique is used as an in-sequence recooling technique after a measurement and therefore the cooling time has to be short compared to the qubit coherence time. Therefore, we adjust the cooling parameters to achieve a faster cooling rate at the cost of a higher steady state phonon number of $\langle n \rangle = 0.5$ after a cooling time of $200 \mu s$. Figure 14 compares the cooling rates of the two distinct cooling techniques.

In first-order Lamb-Dicke approximation ($\eta \ll 1$), the phonon number of the remaining motional modes does not affect the dynamics of the system. But as a second order effect, the occupation of these modes

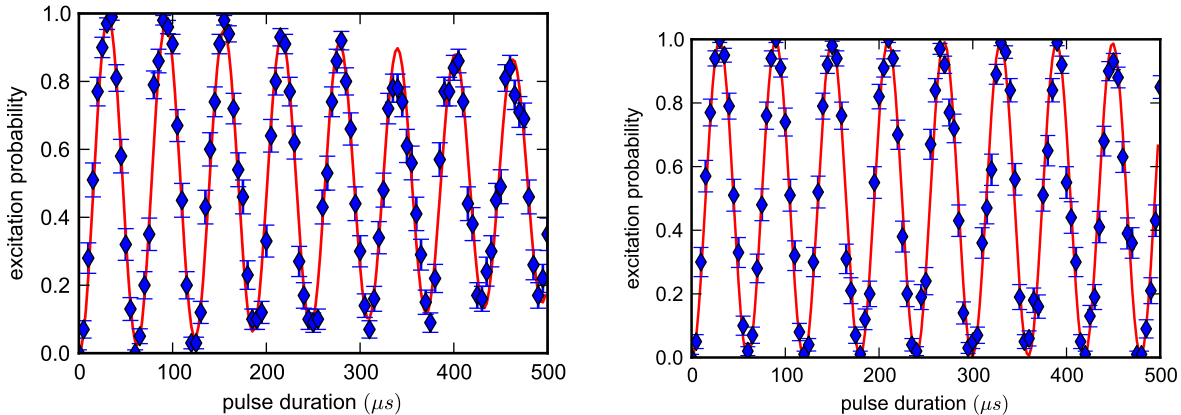


Figure 15. Rabi oscillations in a three-qubit register illustrating the influence of thermal occupation of the motional modes when a) only the COM mode is cooled and b) all three axial modes are cooled.

alters the coupling strength of the ion to the light, which causes an effective fluctuation of the Rabi frequency as the phonon number follows a thermal distribution after cooling [9, 60]. These fluctuations are equivalent to intensity fluctuations of the driving laser and cause a damping of the contrast of the Rabi oscillations. This is illustrated in figure 15a) which shows Rabi oscillations in a register of three ions where sideband cooling was applied only to the COM mode. In contrast, figure 15b) shows the same oscillations where all three axial modes were cooled subsequently and the damping of the oscillations is reduced. An N ion crystal features $3N$ modes and thus cooling all modes in a crystal gets increasingly difficult for larger registers. Fortunately, cooling all modes of the crystal is not always necessary because the mean-phonon number decreases with increasing mode energy. Therefore we cool only the three modes corresponding to the lowest energies to effectively suppress this error source for up to 10 ions. In our setup this error source is smaller on the addressed beam than the global beam, because the Lamb-Dicke parameter is smaller as described in section 2.

3.2.2. Coherent manipulation Additional errors occurring during the coherent manipulation of the quantum information are mainly due to (i) laser intensity fluctuations (ii) crosstalk and (iii) the limited coherence of the motional mode.

Intensity fluctuations of the laser light manipulating the ions lead to a fluctuating Rabi frequency and thus decrease the fidelity of the operations. Measuring the fluctuations of the light field with a photodiode indicates that the fluctuations have relevant timescales on the order of seconds to minutes. We assume therefore that the major sources are (i) fluctuations of the coupling efficiency into a single-mode optical fiber, (ii) thermal effects in acousto-optical devices, (iii) polarization drifts in the fiber, which translate into a varying intensity after polarization defining optics, and (iv) beam pointing instability of the laser light with respect to the ion. These intensity fluctuations can be measured directly on the ions by inserting AC-Stark shift operations with varying length into a Ramsey experiment as sketched in figure 16a). The AC-Stark shift operations convert intensity fluctuations directly into phase fluctuations and thus the same Ramsey techniques as for characterizing phase-noise can be used to measure them. The timescale of the intensity fluctuations is slow compared to the required time for taking 100 repetitions of the sequence

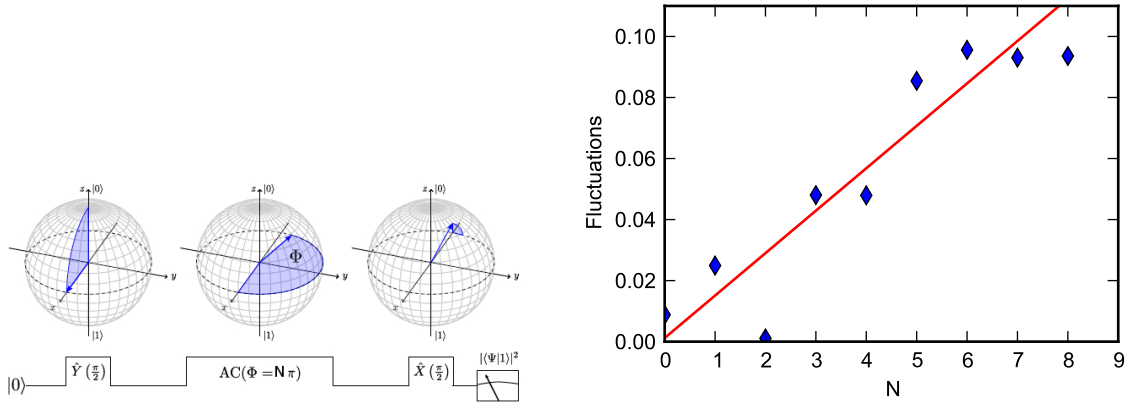


Figure 16. a) Measurement scheme for the slow intensity fluctuations with Ramsey type experiments. Multiple (N -times) rotations around the z-axis of the Bloch sphere are introduced into a Ramsey experiment translating intensity fluctuations into additional noise on the excitation probability. b) Measured state probability fluctuations Δp for multiple N where the slope is fitted to be 0.013(1) leading to effective intensity fluctuations of $\langle\Delta I/I\rangle_N = 0.41(6)\%$.

and thus they cause excess fluctuations of the measured excitation probabilities rather than a coherence decay.

These excess fluctuations can be determined by comparing the standard deviation of the measured data with the expected projection noise $\Delta p^2 = \Delta_{proj}^2 + \Delta_{excess}^2$. This excess noise in the state probability can be translated into fluctuations of the rotation angle via error propagation. We choose the rotation angle to be $\theta = N\pi$ with N being an integer yielding $\Delta\theta/\theta = \Delta p_{excess}/\pi N$ and perform this analysis up to $N = 8$. The measured state probability fluctuations are then analyzed with a linear fit as shown in figure 16b). From this, the relative fluctuations of the rotation angles are determined which are directly equivalent to the relative fluctuation of the Rabi frequency $\Delta\theta/\theta = \Delta\Omega/\Omega$. For the AC-Stark shift operations the Rabi frequency is directly proportional to the laser intensity yielding $\Delta\Omega/\Omega = \Delta I/I$. From the fitted data we can identify the average laser fluctuations to be $\langle\Delta I/I\rangle_N = 0.41(6)\%$.

An error source that affects the register when performing addressed single-qubit operations is crosstalk where due to the finite width of the addressing laser, along with the desired ion, its neighboring ions are affected. This addressing error is characterized by the ratio of the flopping frequency of the addressed ion i to the flopping frequency of the ion j : $\epsilon_{i,j} = \Omega_i^2/\Omega_j^2$. The addressed operation, when addressing ion i , can then be described by $S_z^{(i)}(\theta) = \exp(i\theta \sum_j \sigma_z^{(j)} \epsilon_{i,j})$ where ϵ is the addressing matrix describing the crosstalk. The magnitude of the error can then be bounded by the maximum off-diagonal element of this matrix $\epsilon_{max} = \max_{i \neq j} \epsilon_{i,j}$. In figure 17 an example of excessive crosstalk in a three ion register is shown with $\epsilon_{max} = 22/121 = 18\%$. Typically, the maximum crosstalk on the addressed AC-Stark operations is $\epsilon_{max} < 3\%$ for up to 8 ions where crosstalk between more distant ions is typically smaller than 10^{-3} . Note that this error is coherent, and thus can be undone if the whole addressing matrix is known. Thus, the compensation of the crosstalk can be integrated into the numerical optimization algorithm generating the sequence of operations if the crosstalk is constant over time.

The presented error sources affect both, entangling as well as non-entangling operations. A loss of

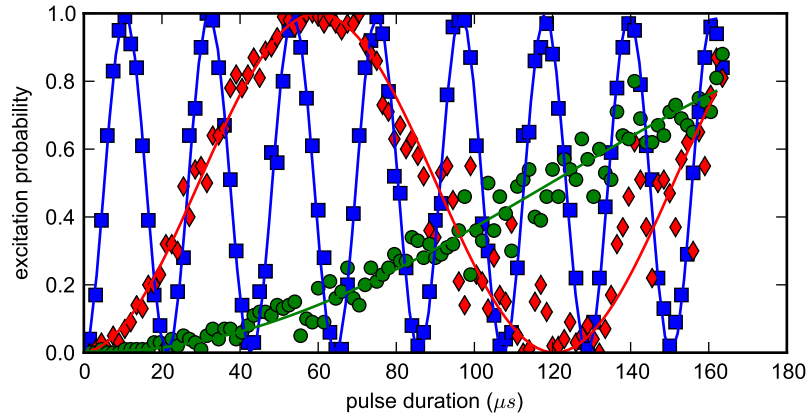


Figure 17. Illustration of the crosstalk between neighboring qubits where the middle ion (blue rectangles) is addressed. The fitted Rabi oscillation periods are $22\mu s$ for the addressed ion 2, $121\mu s$ for ion 1 (red diamonds), and $464\mu s$ for ion 3 (green circles).

coherence on the motional mode does not affect non-entangling operations. However, the entangling MS operation require coherences between different motional states, which can be decreased by (i) fluctuations of the static voltages defining the trap frequencies and (ii) heating of the ion string. The coherence time of the motional mode can be determined by performing a Ramsey type experiment which is only sensitive to the phase between two different motional states. This is possible by using a superposition of two motional states $1/\sqrt{2}(|S, 0\rangle + |S, 1\rangle)$ instead of a superposition of the electronic state $1/\sqrt{2}(|S\rangle + |D\rangle)$ [61]. The motional coherence is then measured analogous to the qubit storage time and yields an exponential decay with time constant $\tau_{motion} = 110(20)\text{ms}$. This coherence time is sufficiently long to allow high fidelity operations to be performed [11].

3.2.3. Measurement The dominant source of errors in the measurement of the qubit is given by spontaneous decay from the $3D_{5/2}$ state during the measurement process as well as stray-light. Both errors affect the measurement if the qubit is projected into the $|0\rangle = 3D_{5/2}(m = -1/2)$ state. The stray-light is modeled by a Poissonian distribution with a mean value of typically 1 counts/ms. The decay from the $3D_{5/2}$ state can also be included which slightly modifies this distribution (for details see reference [62]). For a ion being projected into the $|1\rangle (4S_{1/2})$ state, the photon distribution corresponds to a simple Poissonian distribution with typically 50 counts/ms. The detection error corresponds then to the overlap of the probability distributions for a bright and a dark ion which can be well below 10^{-3} . The results from the CCD camera detection overlaps with the PMT outcome at a level of better than 99.3% [63].

3.3. Estimating the effect of noise on an algorithm

In order to determine the effect of the individual error sources for a given sequence of operations, a numerical simulation including them has to be performed on a classical computer, which is in general a tedious task – even for a few ions. We developed and use a numerical modeling software named

Error source	Overlap with ideal state
All	77 %
Crosstalk	95%
Dephasing	84 %
Intensity fluctuations	99%
Spectator modes	94%

Table 4. Results for the numerical simulation of a quantum simulation algorithm where smaller overlap means a larger error. In order to identify the dominant error source, the simulation is performed multiple times with only a single active error source. From the results one can infer that dephasing is the dominant source of errors. The errors caused by motional heating, imperfect optical pumping and spontaneous decay are negligible.

“Trapped Ion Quantum Computing - Simulation Program with Integrated Circuit Emphasis” (TIQC-SPIICE) [64]. It follows a Monte Carlo approach which simulates multiple random trajectories of varying parameters [65, 66] where each trajectory yields a pure final state. The ensemble average over all trajectories is then the density operator corresponding to the simulated state of the system.

In the following we investigate two algorithms which show different susceptibility to the individual noise sources. The algorithms will not be explained in detail here as we focus on the effect of the different noise sources on the fidelity of the final state. As a first algorithm we investigate a single timestep of an open-system quantum simulator (details on the algorithm are given in reference [67]). This algorithm acts on two system qubits but requires an additional auxiliary qubit whose state can be neglected. We simulate its sequence of operations, shown in the appendix, table 10, on a three-ion register using our TIQC-SPIICE program where each simulation run consists of a Monte-Carlo simulation with 15 trajectories. The included noise sources and their magnitudes are: crosstalk between next neighbors of $\epsilon_{neighbor} = 3\%$; Intensity fluctuations are given by $\Delta I/I = 2\%$; Dephasing is characterized by the coherence time $\tau_{coh} = 15\text{ms}$ and the correlation time $\tau_{corr} = 333\mu\text{s}$ as defined in reference [36]. Coupling to spectator modes is modeled by additional intensity fluctuations of 2%. The simulated output state of the two system qubits is then compared with the expected ideal state. The effect for each individual noise source is identified by simulating the sequence multiple times where for each simulation only a single source is affecting the simulation. The simulations for individual error sources indicate that the dominant error source is dephasing as shown in table 4. This is expected because the duration of the sequence of operations is 2 ms which is not short compared to the coherence time of 15 ms. Including all noise sources, the simulation predicts a fidelity with the ideal density matrix of 79% whereas the experimentally measured fidelity is 72%. The overlap of the simulated with the measured density matrix is 94%.

The second simulated algorithm is a fully coherent quantum Fourier transform (QFT) which is treated in more detail in section 4. The sequence of operation as shown in the appendix, table 11, is simulated with identical parameters as the previous algorithm. The simulation predicts a fidelity of 92.6% with the ideal state whereas an experimentally obtained density matrix leads to an overlap of 81(3)%. The results of the simulation for the individual noise sources are shown in table 5 where the biggest contribution is now crosstalk.

Error source	Overlap with ideal state
All	93 %
Crosstalk	95%
Dephasing	98 %
Intensity fluctuations	>99%
Spectator modes	>99%

Table 5. Results of a numerical simulation of a three-qubit QFT algorithm where a smaller overlap means a larger error. Here, the dominant noise source is crosstalk. The errors caused by motional heating, imperfect optical pumping and spontaneous decay are negligible.

4. Example algorithms

In the following we provide examples of how the available toolbox can be employed to realize various quantum algorithms where we focus on building blocks for a realization of Shor’s algorithm to factor a large integer numbers [3, 18]. The part of the algorithm that requires a quantum computer is based on an order-finding algorithm which itself requires the quantum Fourier transform (QFT). This quantum analog of the discrete Fourier transform maps a quantum state vector $|x\rangle = \sum_j x_j |j\rangle$, into the state $|y\rangle = \sum_k y_k |k\rangle$ where the vector $y = (y_1, \dots, y_N) = \mathcal{F}(x)$ is the classical discrete Fourier transform of $x = (x_1, \dots, x_N)$ [18]. It is straightforward to translate this operation into a quantum circuit (see reference [18]) where an example for three qubits is shown in figure 18a). The most straightforward (although not necessarily the most effective) way to implement the QFT is to realize directly the desired unitary using our available operations. With our optimization toolbox as described in section 1 we are able to find an optimized decomposition of the three-qubit QFT consisting of 18 operations as shown in the appendix, table 11. The smallest MS operation in the sequence is $\pi/16$ and thus the MS operations has to be optimized with this rotation angle. A maximally entangling operation is then implemented by applying this operation 8 times subsequently.

We benchmark the QFT by performing a full three-qubit quantum process tomography and find a process fidelity of 72% with the ideal QFT [68]. However, in order to find the best suited measure for the quality of an algorithm, one should consider how the quantum algorithm is embedded in the given problem. The QFT is almost exclusively used as the final building block of larger algorithms and then only the classical information of the final state is needed to determine the algorithm’s performance [69]. The quantum process fidelity is not the optimal measure to benchmark the performance of the QFT as it includes correlations that do not affect the outcome of the algorithm. One would rather choose a measure that utilizes the classical probabilities of the individual output states which can be described by a 2^N vector $p = (p_1, \dots, p_{2^N})$. Such a measure is the squared statistical overlap (SSO) $S(p, q) = (\sum_i \sqrt{p_i q_i})^2$ which is the classical analog of the quantum state fidelity [70]. An alternative suitable measure for the classical information is the statistical distinguishability $D(p, q) = 1 - 1/2 \sum_i |p_i - q_i|$, which is related to the quantum trace distance. These benchmarks are applied to a representative set of input states covering all possible periods. In reference [71], a QFT algorithm was benchmarked using five input states with different period and thus we use similar input states for comparability, as shown in table 6. The classical benchmarks yield on average an SSO of 87% which is considerably higher than the quantum process

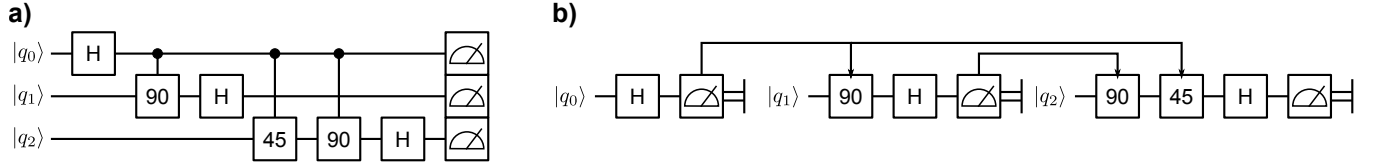


Figure 18. (a) Quantum circuit for a three qubit QFT algorithm. (b) Single-qubit Kitaev version of the QFT. The measurement outcome is stored in a classical memory which controls the subsequent single-qubit rotations.

Input state	Period	SSO	Distinguishability
$1/\sqrt{8} (111\rangle + 110\rangle + \dots + 000\rangle)$	1	77.1	77.1
$1/\sqrt{4} (110\rangle + 100\rangle + 010\rangle + 000\rangle)$	2	78.0	73.3
$1/\sqrt{4} (110\rangle + 100\rangle + 011\rangle + 000\rangle)$	3	90.4	86.4
$1/\sqrt{2} (011\rangle + 000\rangle)$	4	94.8	87.4
$ 000\rangle$	8	97.3	88.1

Table 6. Results for a fully coherent 3 qubit QFT.

fidelity of 72%.

Since the QFT is mainly used as the final block in an algorithm, it can be replaced by the semi-classical QFT that exchanges the quantum-controlled rotations by a measurement and a classically controlled rotation [69, 71]. This requires the measurement of each qubit to be performed before the operations that are controlled by this qubit. In figure 18 the time order of the measurements corresponds to qubit q_0 , q_1 , q_2 . A measurement furthermore destroys all quantum coherence on the qubit and thus it is possible to reuse the physical qubit and store the measurement outcome on a classical computer. This allows a semi-classical QFT to be performed on a single qubit as sketched in figure 18b) which is known as the Kitaev QFT [72]. Note that it is not possible to generate an entangled input state with this version of the QFT and thus the Kitaev QFT is more restricted than the semi-classical QFT. Furthermore, the ability to measure and reset the qubit within the algorithm is required, which is possible with our extended set of operations. In ion-trap systems, in-sequence measurements notably disturb the motional state of the ion string and thus it is advisable to make the measurement as short as possible. In this case we chose a measurement duration of $150\mu s$ which still allows for a detection fidelity of 99% [73]. In order to achieve high fidelity operations after such a measurement it appears necessary to recool the COM mode with the Raman cooling technique as described in section 1. In the special case of the single-qubit QFT however only local operations are required after a measurement which can furthermore be implemented with the addressed beam. Due to the small Lamb-Dicke parameter, the quality of the single-qubit operations is not notably affected by the thermal occupation of the COM and the spectator modes after the measurements and thus recooling is not required. In table 7 the outcome for the single qubit QFT is shown for the non-entangled input states used before, leading to an average SSO of 99.6%. As expected, the single-qubit Kitaev QFT clearly performs better than the fully coherent QFT.

One of the important algorithms that is compatible with the presented Kitaev single-qubit QFT is the order-finding algorithm which is able to determine the order of a permutation operation efficiently [18]. A permutation operation $\pi(y)$ has order k if k -times application of the operations results in the identity:

Input state	Period	SSO	Distinguishability
$1/\sqrt{4} (000\rangle + 100\rangle + 010\rangle + 110\rangle)$	2	99.5	94.5
$1/\sqrt{2} (100\rangle + 000\rangle)$	4	99.6	96.4
$ 000\rangle$	8	99.7	95.6

Table 7. Results for the semiclassical Kitaev single qubit QFT.

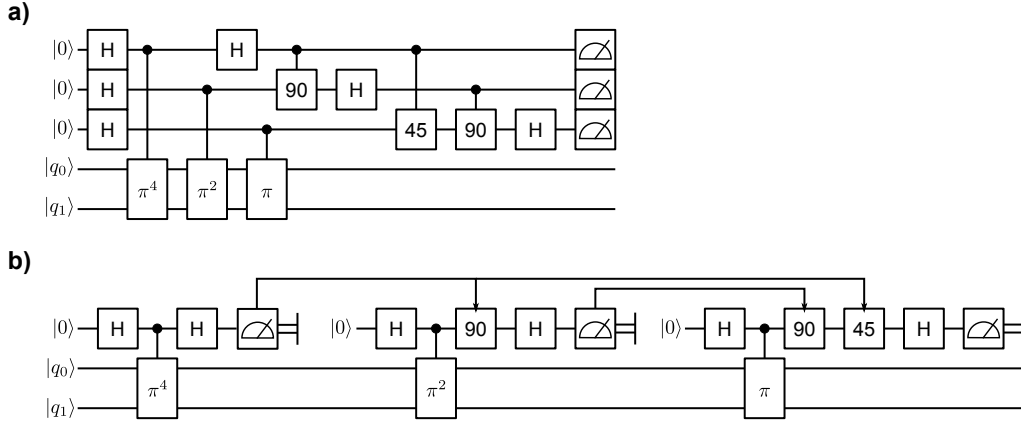


Figure 19. order finding algorithm for a two qubit permutation operation in a) fully coherent and b) Kitaev version.

$\pi(y)^k = y$, where y is a decimal representation of the n -qubit input state vector $|q_n \dots q_0\rangle$. The algorithm splits the available quantum register in two parts: (i) a register where the permutation operation is applied and (ii) a QFT register that is initially prepared in an equal superposition state. The qubits from the QFT register control whether the permutation operations are applied. This operation is analogous to a CNOT operation where instead of the NOT operation the permutation operation is controlled. The k -th qubit from the QFT register controls the permutation operations $\pi(y)^l$ with $l = 2^k$ as shown in figure 19a). With this algorithm it is possible to use the single-qubit QFT to reduce the number of required qubits from 5 to 3 where the resulting quantum circuit is shown in figure 19b).

We seek to implement the optimized order-finding algorithm using permutations on two qubits as a proof-of-concept experiment. The permutation operation is given by a unitary operation where we implemented the operations shown in table 8 which span orders from 2 to 4. It becomes clear that the order of the permutation can depend on the input state as, for example, $\pi_1(y)$ has order one for input states $y = |0\rangle, |2\rangle$ and order two for $y = |1\rangle, |3\rangle$. On the other hand, $\pi_2(y)$ shows order two regardless of the input state. The complexity of the algorithm depends on the investigated permutation operation, as the controlled permutation operations require entangling operations. The number of required operations for the individual permutation operations are presented in table 8 and the sequences of operations can be found in the appendix. In contrast to the single-ion QFT as presented above, the use of entangling operations after measuring the QFT qubit is required. This makes it necessary to recool the ion string within the sequence, where we employ the Raman recooling technique as described in section 1. We choose a recooling time of $800\mu s$ as this proved to provide a good balance between remaining excitation of the COM mode and additional phase damping due to the cooling time [73].

The output of the algorithm is again classical and thus the classical probabilities for measuring the state

y	$\pi_1(y)$	$\pi_2(y)$	$\pi_3(y)$	$\pi_4(y)$
$ 0\rangle$	$ 0\rangle$	$ 1\rangle$	$ 0\rangle$	$ 3\rangle$
$ 1\rangle$	$ 3\rangle$	$ 0\rangle$	$ 3\rangle$	$ 0\rangle$
$ 2\rangle$	$ 2\rangle$	$ 3\rangle$	$ 1\rangle$	$ 1\rangle$
$ 3\rangle$	$ 1\rangle$	$ 2\rangle$	$ 2\rangle$	$ 2\rangle$
max(order)	2	2	3	4
no. of operations $\pi(y)$	11	10	23	24
no. of operations $\pi(y)^2$	-	-	17	10

Table 8. Representative unitary permutation operations for order 2 to 4 which were used as examples for the order-finding algorithm. The number of operations for applying the operation once and twice are also shown. The sequence of operation for the controlled permutation operations are presented in the appendix.

Order	Permutation operation	SSO	Distinguishability
1	$\pi_1(0\rangle)$	75.3(7)	75.3(7)
2	$\pi_2(0\rangle)$	86.4(6)	86.5(6)
3	$\pi_3(1\rangle)$	85.9(6)	70.3(8)
4	$\pi_4(0\rangle)$	91.6(5)	90.7(6)

Table 9. Results for the semiclassical Kitaev order finding algorithm using the permutation operations defined in table 8.

$|j\rangle$ are sufficient to infer the quality of the operation. Figure 20 shows the classical probabilities of the basis states for all permutation operations where the experimental results (blue bars) are compared with the expected ideal probabilities (red bars) and estimated probabilities from TIQC-SPICE simulations (green bars). Again the implementation is benchmarked with the classical SSO and distinguishability measures as presented in table 9 yielding an average SSO of 80.7%. The original problem is finding the correct permutation and therefore one could think of using a classical algorithm to find the most likely order for a given outcome. However, finding such an efficient evaluation is beyond the scope of this work.

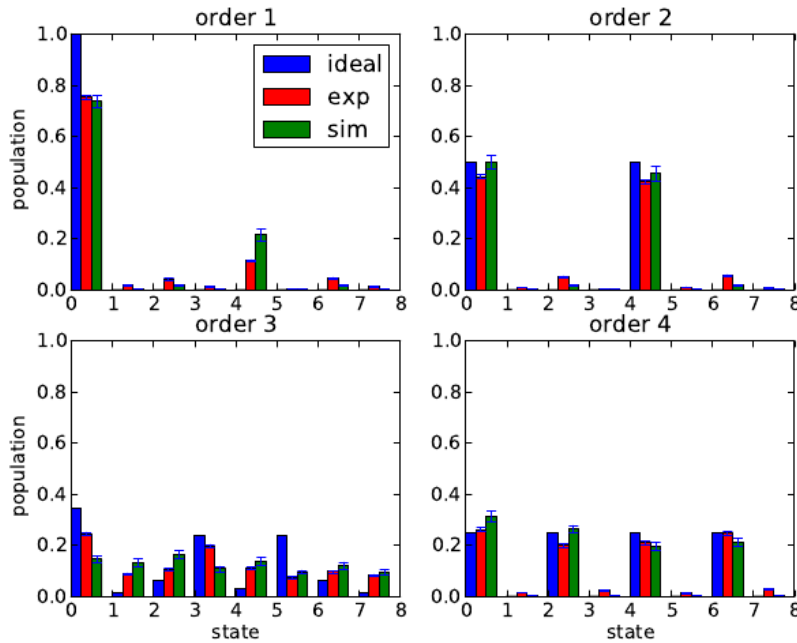


Figure 20. State probabilities for the order finding algorithm for the permutation operations $\pi_1 \dots \pi_4$. The ideal probabilities (blue), experimental results (red) and predictions from a classical simulation (green) are shown.

5. Conclusion and Outlook

In conclusion we have presented a small-scale quantum information processor based on trapped $^{40}\text{Ca}^+$ ions. A set of operations beyond coherent operations, that is suitable for implementing arbitrary Markovian processes, has been introduced. The major noise sources of the system acting on a qubit memory and during operations have been analyzed and their influence on different algorithms have been discussed. It has been shown that the dominant source of errors depends on the actual sequence of operations. We used the entire set of operations to realize an efficient implementation of the order-finding algorithm. Here, we have been able to reduce the number of required qubits in the sense that only a single qubit is required for the entire QFT register in the algorithm. We envision, that these techniques will be the building blocks in a scalable implementation of Shor's factoring algorithm. Furthermore we hope that the presented methods for characterizing the noise sources will lead to successful strategies for reducing the error rate in complex algorithms paving the way to fault-tolerant quantum computation.

Acknowledgments

We thank J. Home and M. Müller for helpful feedback on the manuscript. We gratefully acknowledge support by the Austrian Science Fund (FWF), through the SFB FoQus (FWF Project No. F4002-N16), by the European Commission (AQUTE), as well as the Institut für Quantenoptik und Quanteninformation GmbH. This research was funded by the Office of the Director of National Intelligence (ODNI), Intelligence Advanced Research Projects Activity (IARPA), through the Army Research Office grant

W911NF-10-1-0284. All statements of fact, opinion or conclusions contained herein are those of the authors and should not be construed as representing the official views or policies of IARPA, the ODNI, or the U.S. Government.

References

- [1] Calderbank A R and Shor P W. *Physical Review A*, 54(2):1098–1105, 1996.
- [2] Shor P W. *Foundations of Computer Science*, 96, 1996.
- [3] Shor P W. *Foundations of Computer Science, 1994 Proceedings., 35th Annual Symposium on*, pages 124–134, 1994.
- [4] Steane A M. *Physical Review Letters*, 77(5):793–797, 1996.
- [5] Blatt R and Wineland D. *Nature*, 453(7198):1008–1015, 2008.
- [6] Clarke J and Wilhelm F K. *Nature*, 453(7198):1031–1042, 2008.
- [7] Bloch I. *Nature*, 453(7198):1016–1022, 2008.
- [8] Cirac J I and Zoller P. *Physical Review Letters*, 74(20):4091–4094, 1995.
- [9] Wineland D. *Journal of Research of the National Institute of Standards and Technology*, 103, 1997.
- [10] Naegerl H C. *Ion Strings for Quantum Computing*. Ph.D. thesis, Universität Innsbruck, 1998.
- [11] Schmidt-Kaler F, Gulde S, Riebe M, Deuschle T, Kreuter A, et al. *Journal of Physics B: Atomic, Molecular and Optical Physics*, 36(3):623–636, 2003.
- [12] Roos C, Zeiger T, Rohde H, Nägerl H C, Eschner J, et al. *Physical Review Letters*, 83(23):4713–4716, 1999.
- [13] Itano W M, Bergquist J C, Bollinger J J, Gilligan J M, Heinzen D J, et al. *Physical Review A*, 47(5):3554–3570, 1993.
- [14] Eschner J, Morigi G, Schmidt-Kaler F, and Blatt R. *Journal of the Optical Society of America B*, 20(5):1003–1015, 2003.
- [15] Rohde H, Gulde S T, Roos C F, Barton P A, Leibfried D, et al. *Journal of Optics B: Quantum and Semiclassical Optics*, 3(1):S34–S41, 2001.
- [16] Marzoli I, Cirac J I, Blatt R, and Zoller P. *Physical Review A*, 49:2771–2779, 1994.
- [17] Riebe M, Chwalla M, Benhelm J, Häffner H, Hänsel W, et al. *New Journal of Physics*, 9(7):211, 2007.
- [18] Nielsen M A and Chuang I L. *Quantum Computation and Quantum Information (Cambridge Series on Information and the Natural Sciences)*. Cambridge University Press, first edition, 2004.
- [19] Benhelm J, Kirchmair G, Roos C F, and Blatt R. *Nature Physics*, 4(6):463–466, 2008.
- [20] Sørensen A and Mølmer K. *Physical Review A*, 62(2):022311, 2000.
- [21] Sørensen A and Mølmer K. *Physical Review Letters*, 82(9):1971–1974, 1999.
- [22] Häffner H, Gulde S, Riebe M, Lancaster G, Becher C, et al. *Physical Review Letters*, 90(14):143602, 2003.
- [23] Kirchmair G, Benhelm J, Zähringer F, Gerritsma R, Roos C F, et al. *New Journal of Physics*, 11(2):023002, 2009.
- [24] Müller M, Hammerer K, Zhou Y L, Roos C F, and Zoller P. *New Journal of Physics*, 13(8):085007, 2011.
- [25] Khaneja N, Reiss T, Kehlet C, Schulte-Herbrüggen T, and Glaser S J. *Journal of Magnetic Resonance*, 172(2):296–305, 2005.
- [26] Nebendahl V, Häffner H, and Roos C F. *Physical Review A*, 79(1):012312, 2009.
- [27] Kielpinski D, Monroe C, and Wineland D J. *Nature*, 417(6890):709–711, 2002.
- [28] Barreiro J T, Schindler P, Guhne O, Monz T, Chwalla M, et al. *Nature Physics*, 6(12):943–946, 2010.
- [29] Verstraete F, Wolf M M, and Ignacio Cirac J. *Nature Physics*, 5(9):633–636, 2009.
- [30] Diehl S, Micheli A, Kantian A, Kraus B, Buchler H P, et al. *Nature Physics*, 4(11):878–883, 2008.
- [31] Nigg D, Barreiro J T, Schindler P, Mohseni M, Monz T, et al. *Physical Review Letters*, 110:060403, 2013.
- [32] Schindler P, Barreiro J T, Monz T, Nebendahl V, Nigg D, et al. *Science*, 332(6033):1059–1061, 2011.
- [33] Barreiro J T, Müller M, Schindler P, Nigg D, Monz T, et al. *Nature*, 470(7335):486–491, 2011.
- [34] Baggio G, Ticozzi F, and Viola L. In *Decision and Control (CDC), 2012 IEEE 51st Annual Conference on*, pages 1072–1077. IEEE, 2012.
- [35] Lloyd S and Viola L. *Physical Review A*, 65:010101, 2001.
- [36] Monz T, Schindler P, Barreiro J T, Chwalla M, Nigg D, et al. *Physical Review Letters*, 106(13):130506, 2011.
- [37] Berkeland D J, Miller J D, Bergquist J C, Itano W M, and Wineland D J. *Journal of Applied Physics*, 83(10):5025–5033, 1998.
- [38] Chwalla M, Benhelm J, Kim K, Kirchmair G, Monz T, et al. *Physical Review Letters*, 102(2):023002, 2009.
- [39] Chwalla M. *Precision spectroscopy with $^{40}\text{Ca}^+$ ions in a Paul trap*. Ph.D. thesis, Universität Innsbruck, 2009.
- [40] Gulde S. *Experimental Realization of Quantum Gates and the Deutsch-Jozsa Algorithm with Trapped Ca Atoms*. Ph.D. thesis, Universität Innsbruck, 2003.
- [41] Pham P. *A general-purpose pulse sequencer for quantum computing*. Master’s thesis, Massachusetts institute of technology, 2005.

- [42] Alnis J, Matveev A, Kolachevsky N, Th, and Hänsch T W. *Physical Review A*, 77:053809, 2008.
- [43] Tóth G, Wicczorek W, Gross D, Krischek R, Schwemmer C, et al. *Physical Review Letters*, 105:250403, 2010.
- [44] Burrell A H, Szwer D J, Webster S C, and Lucas D M. *Physical Review A*, 81(4):040302, 2010.
- [45] Barton P A, Donald C J S, Lucas D M, Stevens D A, Steane A M, et al. *Physical Review A*, 62(3):032503, 2000.
- [46] Tommaseo G, Pfeil T, Revalde G, Werth G, Indelicato P, et al. *The European Physical Journal D - Atomic, Molecular, Optical and Plasma Physics*, 25(2):113–121, 2003.
- [47] Szwer D J, Webster S C, Steane A M, and Lucas D M. *Journal of Physics B: Atomic, Molecular and Optical Physics*, 44(2):025501, 2011.
- [48] Sagi Y, Almog I, and Davidson N. *Physical Review Letters*, 105:053201, 2010.
- [49] Barthel C, Medford J, Marcus C M, Hanson M P, and Gossard A C. *Physical Review Letters*, 105:266808, 2010.
- [50] de Lange G, Wang Z H, Risté D, Dobrovitski V V, and Hanson R. *Science*, 330(6000):60–63, 2010.
- [51] Ryan C A, Hodges J S, and Cory D G. *Physical Review Letters*, 105(20):200402, 2010.
- [52] Du J, Rong X, Zhao N, Wang Y, Yang J, et al. *Nature*, 461(7268):1265–1268, 2009.
- [53] Biercuk M J, Uys H, VanDevender A P, Shiga N, Itano W M, et al. *Nature*, 458(7241):996–1000, 2009.
- [54] Kotler S, Akerman N, Glickman Y, Keselman A, and Ozeri R. *Nature*, 473(7345):61–65, 2011.
- [55] Bylander J, Gustavsson S, Yan F, Yoshihara F, Harrabi K, et al. *Nature Physics*, 7(7):565–570, 2011.
- [56] Monz T, Kim K, Villar A S, Schindler P, Chwalla M, et al. *Physical Review Letters*, 103(20):200503, 2009.
- [57] Häffner H, Schmidt-Kaler F, Hänsel W, Roos C F, Körber T, et al. *Applied Physics B: Lasers and Optics*, 81(2):151–153, 2005.
- [58] Monz T. *Quantum information processing beyond ten ion-qubits*. Ph.D. thesis, Universität Innsbruck, 2011.
- [59] Roos C F, Chwalla M, Kim K, Riebe M, and Blatt R. *Nature*, 443(7109):316–319, 2006.
- [60] Poschinger U, Walther A, Hettrich M, Ziesel F, and Schmidt-Kaler F. *Applied Physics B: Lasers and Optics*, 107(4):1159–1165, 2012.
- [61] Roos C F, Monz T, Kim K, Riebe M, Häffner H, et al. *Physical Review A*, 77(4):040302, 2008.
- [62] Roos C F. *Controlling the quantum state of trapped ions*. Ph.D. thesis, Universität Innsbruck, 2000.
- [63] Riebe M. *Preparation of entangled states and quantum teleportation with atomic qubits*. Ph.D. thesis, Universität Innsbruck, 2005.
- [64] Wang S X. *Quantum Gates, Sensors, and Systems with Trapped Ions*. Ph.D. thesis, Massachusetts institute of technology, 2012.
- [65] Dalibard J, Castin Y, and Mølmer K. *Physical Review Letters*, 68(5):580–583, 1992.
- [66] Mølmer K, Castin Y, and Dalibard J. *Journal of the Optical Society of America B*, 10(3):524–538, 1993.
- [67] Schindler P, Muller M, Nigg D, Barreiro J T, Martinez E A, et al. *Nature Physics*, 9(6):361–367, 2013.
- [68] Chuang I and Nielsen M A. *Journal of Modern Optics*, 44(11):2455–2467, 1997.
- [69] Griffiths R B and Niu C S. *Physical Review Letters*, 76(17):3228–3231, 1996.
- [70] Fuchs C A. *arxiv:quant-ph/9601020*, 1996.
- [71] Chiaverini J, Britton J, Leibfried D, Knill E, Barrett M D, et al. *Science*, 308(5724):997–1000, 2005.
- [72] Martin-Lopez E, Laing A, Lawson T, Alvarez R, Zhou X Q, et al. *Nature Photonics*, 6(11):773–776, 2012.
- [73] Schindler P, Monz T, Nigg D, Barreiro J T, Martinez E A, et al. *Physical Review Letters*, 110:070403, 2013.

6. Appendix

Number	Pulse	Number	Pulse
1	$S_z^{(1)}(1.5\pi)$	11	$MS_{1.5\pi}(0.5\pi)$
2	$R_\pi(1.5\pi)$	12	$S_z^{(3)}(1.75\pi, 2)$
3	$MS_\pi(0.25)$	13	$MS_{2.25\pi}(0.5\pi)$
4	$S_z^{(2)}(\pi)$	14	$R_{1.75\pi}(0.5\pi)$
5	$MS_\pi(0.875\pi)$	15	$R_{2.25\pi}(0.5\pi)$
6	$S_z^{(3)}(\pi)$	16	$MS_{2.25\pi}(0.25\pi)$
7	$MS_\pi(0.125\pi)$	17	$S_z^{(3)}(1.5\pi)$
8	$S_z^{(3)}(\pi)$	18	$S_z^{(2)}(1.0\pi)$
9	$R_{0.5\pi}(0.5\pi)$	19	$R_{2.25\pi}(0.5\pi)$
10	$S_z^{(3)}(0.5\pi)$		

Table 10. Sequence of operations for the algorithm used for an open system quantum simulator [67].

Number	Pulse	Number	Pulse
1	$R_\pi(\pi/2)$	10	$R_{\pi/2}(3\pi/16)$
2	$S_z^{(2)}(\pi)$	11	$S_z^{(2)}(3\pi/2)$
3	$S_z^{(3)}(\pi/2)$	12	$R_{\pi/2}(\pi/4)$
4	$MS_{\pi/2}(\pi/8)$	13	$MS_{\pi/2}(\pi/8)$
5	$S_z^{(3)}(\pi)$	14	$S_z^{(3)}(\pi)$
6	$MS_{\pi/2}(\pi/16)$	15	$MS_{\pi/2}(\pi/8)$
7	$R_{-\pi/2}(\pi/2)$	16	$S_z^{(1)}(\pi/2)$
8	$S_z^{(2)}(\pi)$	17	$S_z^{(2)}(\pi)$
9	$MS_{\pi/2}(3\pi/16)$	18	$R_\pi(\pi/2)$

Table 11. Sequence of operations for the fully coherent QFT operation on three qubits.

Number	Pulse	Number	Pulse
1	$R_{\pi/2}(\pi/2)$	7	$MS_0(\pi/4)$
2	$S_z^{(3)}(7\pi/4)$	8	$S_z^{(3)}(3\pi/2)$
3	$MS_0(\pi/2)$	9	$MS_0(\pi/2)$
4	$R_\pi(\pi/2)$	10	$R_{-\pi}(\pi/2)$
5	$S_z^{(3)}(\pi/2)$	11	$R_{-\pi/2}(\pi/2)$
6	$R_\pi(\pi/4)$		

Table 12. Sequence of the controlled $\pi_1(y)$ permutation operation.

Number	Pulse	Number	Pulse
1	$R_\pi(\pi/2)$	5	$MS_0(\pi/4)$
2	$S_z^{(1)}(3\pi/2)$	6	$S_z^{(1)}(3\pi/2)$
3	$MS_0(\pi/2)$	7	$R_\pi(\pi/2)$
4	$R_\pi(\pi/2)$	8	$S_z^{(2)}(\pi)$

Table 13. Sequence of the controlled $\pi_2(y)$ permutation operation.

Number	Pulse	Number	Pulse
1	$S_z^{(3)}(\pi/2)$	13	$S_z^{(2)}(\pi/2)$
2	$R_\pi(3\pi/2)$	14	$S_z^{(3)}(3\pi/2)$
3	$S_z^{(3)}(\pi/2)$	15	$MS_0(3\pi/4)$
4	$MS_0(\pi/4)$	16	$R_{-\pi/2}(0.196\pi)$
5	$R_{-\pi}(5\pi/2)$	17	$S_z^{(2)}(2\pi/3)$
6	$S_z^{(1)}(3\pi/2)$	18	$R_{\pi/2}(0.196\pi)$
7	$R_\pi(\pi/2)$	19	$R_\pi(\pi/4)$
8	$R_{\pi/2}(\pi/4)$	20	$MS_0(\pi/2)$
9	$S_z^{(2)}(\pi)$	21	$S_z^{(2)}(7\pi/4)$
10	$R_{\pi/2}(\pi/4)$	22	$R_{\pi/2}(\pi/2)$
11	$MS_0(\pi/2)$	23	$S_z^{(1)}(\pi/2)$
12	$S_z^{(1)}(\pi)$		

Table 14. Sequence of the controlled $\pi_3(y)$ permutation operation.

Number	Pulse	Number	Pulse
1	$R_{\pi/2}(\pi/2)$	10	$S_z^{(2)}(3\pi/2)$
2	$S_z^{(2)}(\pi/4)$	11	$MS_0(\pi/2)$
3	$R_{-\pi}(\pi/2)$	12	$S_z^{(3)}(3\pi/2)$
4	$MS_0(\pi/2)$	13	$R_\pi(\pi/4)$
5	$S_z^{(2)}(3\pi/2)$	14	$MS_0(\pi/4)$
6	$MS_0(3\pi/4)$	15	$S_z^{(1)}(3\pi/2)$
7	$R_\pi(\pi/4)$	16	$S_z^{(2)}(3\pi/2)$
8	$S_z^{(3)}(\pi/4)$	17	$R_{-\pi}(\pi/2)$
9	$R_\pi(\pi/2)$		

Table 15. Sequence of the controlled $\pi_3^2(y)$ permutation operation.

Number	Pulse	Number	Pulse
1	$R_{-\pi}(\pi/2)$	13	$R_{-\pi/2}(0.196\pi)$
2	$R_{\pi/2}(\pi)$	14	$S_z^{(1)}(4\pi/3)$
3	$S_z^{(1)}(3\pi/2)$	15	$S_z^{(3)}(1.905\pi)$
4	$MS_0(7\pi/8)$	16	$R_{\pi/2}(0.196\pi)$
5	$S_z^{(3)}(\pi)$	17	$R_{-\pi}(\pi/4)$
6	$MS_0(\pi/8)$	18	$R_{-\pi/2}(\pi/2)$
7	$R_{\pi/2}(\pi/2)$	19	$MS_0(\pi/2)$
8	$R_{-\pi}(3\pi/2)$	20	$S_z^{(2)}(\pi/3)$
9	$S_z^{(1)}(3\pi/2)$	21	$MS_0(\pi/2)$
10	$S_z^{(2)}(\pi/2)$	22	$S_z^{(3)}(1.905\pi)$
11	$MS_0(3\pi/4)$	23	$R_{\pi/2}(\pi/2)$
12	$S_z^{(3)}(1.33\pi)$	24	$S_z^{(3)}(7\pi/4)$

Table 16. Sequence of the controlled $\pi_4(y)$ permutation operation.

Number	Pulse	Number	Pulse
1	$R_{\pi}(\pi/2)$	6	$R_{\pi}(\pi/4)$
2	$S_z^{(1)}(3\pi/2)$	7	$MS_0(\pi/4)$
3	$MS_0(\pi/4)$	8	$S_z^{(1)}(3\pi/2)$
4	$R_{\pi}(\pi/4)$	9	$R_{\pi}(\pi/2)$
5	$S_z^{(2)}(\pi)$	10	$S_z^{(2)}(\pi)$
1	$R_{-\pi}(\pi/2)$	13	$R_{-\pi/2}(0.196\pi)$
2	$R_{\pi/2}(\pi)$	14	$S_z^{(1)}(4\pi/3)$
3	$S_z^{(1)}(3\pi/2)$	15	$S_z^{(3)}(1.905\pi)$
4	$MS_0(7\pi/8)$	16	$R_{\pi/2}(0.196\pi)$
5	$S_z^{(3)}(\pi)$	17	$R_{-\pi}(\pi/4)$
6	$MS_0(\pi/8)$	18	$R_{-\pi/2}(\pi/2)$
7	$R_{\pi/2}(\pi/2)$	19	$MS_0(\pi/2)$
8	$R_{-\pi}(3\pi/2)$	20	$S_z^{(2)}(\pi/3)$
9	$S_z^{(1)}(3\pi/2)$	21	$MS_0(\pi/2)$
10	$S_z^{(2)}(\pi/2)$	22	$S_z^{(3)}(1.905\pi)$
11	$MS_0(3\pi/4)$	23	$R_{\pi/2}(\pi/2)$
12	$S_z^{(3)}(1.33\pi)$	24	$S_z^{(3)}(7\pi/4)$

Table 17. Sequence of the controlled $\pi_4^2(y)$ permutation operation.